Aerodynamic Shape Optimization for Natural Laminar Flow Using a Discrete-Adjoint Approach

Ramy Rashad* and David W. Zingg†

University of Toronto, Toronto, Ontario M3H 5T6, Canada

A framework for the design of natural-laminar-flow airfoils is developed based on multipoint aerodynamic shape optimization capable of efficiently incorporating and exploiting laminar-turbulent transition. A two-dimensional Reynolds-averaged Navier-Stokes (RANS) flow solver making use of the Spalart-Allmaras turbulence model has been extended to incorporate an iterative laminar-turbulent transition prediction methodology. The natural transition locations due to Tollmien-Schlichting instabilities are predicted using the simplified e^N envelope method of Drela and Giles or the compressible form of the Arnal-Habiballah-Delcourt criterion. The RANS solver is subsequently used in a gradient-based sequential quadratic programming shape optimization framework. The transition criteria are tightly coupled into the objective and gradient evaluations. The gradients are obtained using an augmented discrete-adjoint formulation for non-local transition criteria. Robust design over a range of cruise flight conditions is demonstrated through multipoint optimization. Finally, a technique is proposed and demonstrated to enable the design of natural-laminar-flow airfoils with robust performance over a range of critical N-factors – the optimizer is seen to produce transition ramps similar to those used by experienced designers.

I. Introduction and Background

THE current push for sustainable and environmentally responsible aviation requires serious efforts to mitigate the escalating effects of such technology on climate change and natural resources. A clear vision for the efficiency of future transport aircraft – with specific targets for reduced fuel burn, emissions and noise – has been published in the U.S. National Aeronautics Research and Development Plan [1]. As a result, manufacturers and researchers are investigating conventional and unconventional aircraft designs to

*PhD Candidate and AIAA Student Member

†Professor and Director, J. Armand Bombardier Foundation Chair in Aerospace Flight, AIAA Associate Fellow

meet these targets. As part of the effort to reduce fuel burn and emissions, aerodynamicists are assessing the feasibility of natural laminar flow (NLF) as a key enabler of environmentally responsible commercial aviation.

Over the past few decades, designers have become heavily reliant on computational fluid dynamics (CFD) and, more recently, on design optimization tools. Despite this, there remain few NLF applications in the current commercial fleet, with Honda's recent HA-420 business jet [2] and the nacelles on the recent Boeing 787 [3] being among the first, if not the only applications to date. The conservative engineering assumption of *fully-turbulent flow*, which considers the flow to be fully-turbulent right from the leading edge (over the entire wetted area), has been common in CFD, and especially in aerodynamic shape optimization (ASO). While this assumption has allowed for advancements in aerodynamic design, the conservatism leaves something to be desired. Indeed, the development of design tools capable of exploiting laminar-turbulent transition is required to enable the robust design of NLF technology and to provide a means by which we may better understand the design trade-offs involved.

I.A. Transition Prediction in RANS Solvers

The challenges in reliably predicting laminar-turbulent transition continue to limit our ability to compute many aerodynamic flows with accuracy [4]. Consequently, the development of transition prediction methods of varying complexity and fidelity is ongoing. While there are several mechanisms that may lead to transition, the two dominant mechanisms typically encountered in high-speed external aerodynamic flows are Tollmien-Schlichting and crossflow instabilities [5].

The turbulence models used in RANS solvers do not have the stand-alone capability to predict the transition locations in a flow field; in order to predict transition, one must apply a transition criterion. In recent years, several approaches for incorporating transition prediction into RANS solvers have been developed. A review by Arnal *et al.* [6] discusses the various advantages and disadvantages of each approach in detail.

The transition criteria employed by the RANS solvers are typically based on either (i) the e^N criterion or (ii) transition onset functions. To apply the e^N criterion one must first approximate the N-factor curves, representing the amplification ratios of the unstable frequencies of the disturbances in the boundary layer. Transition is assumed to occur when the maximum local N-factor has exceeded some critical value (N_{crit}). Values for N_{crit} must be specified *a priori* based on the disturbance environment and/or experimental calibration.

Examples of transition criteria based on a transition onset function are Michel, Granville, $H-Re_x$, Abu-Ghannam and Shaw, Gleyzes-Habiballah and Arnal-Habiballah-Delcourt [7–9]. Each has its range

of applicability and limitations. These criteria typically compare the boundary-layer properties or related quantities (such as Re_θ) to an empirically calibrated transition onset function (such as $Re_{\theta_{\mathrm{tr}}}$). The transition point is the first point at which, for example, $Re_\theta \geq Re_{\theta_{\mathrm{tr}}}$. The transition onset functions are typically computed from the non-local boundary-layer properties; the exception being the local transport equation approach originally developed by Langtry and Menter [9, 10].

The transport equation approach developed by Langtry and Menter [9, 10] has the advantage of a local formulation in the sense that integrated boundary-layer properties are replaced by local flow quantities. The local approach makes it more straightforward to parallelize and differentiate the code. While the method was originally coupled to the k-ω turbulence model, more recent work by Medida and Baeder [11] as well as Aranake *et al.* [12] has successfully coupled the $\gamma - \widetilde{Re}_{\theta_t}$ model to the Spalart-Allmaras turbulence model. Unlike the transport equation approach, the other approaches in the above list are non-local in their formulation, which has some disadvantages. However, these are being addressed; for example, approaches 1 and 2 have been successfully parallelized and extended to three-dimensional flows by Krimmelbein *et al.* [13], and there is no obstacle to their use in an implicit Newton-Krylov type solver, as demonstrated in this work. There is also no required calibration specific to a particular turbulence model [11]. Over the past decade or so, non-local correlations for crossflow instabilities such as the C_1 criterion have been experimentally validated on transonic swept wings in three dimensions [14]. In the past year, the independent works of Langtry [15] and Krumbein [16] have extended the $\gamma - \widetilde{Re}_{\theta_t}$ approach to include a local crossflow transition criterion. Finally, the modular implementation of the transition prediction framework presented here facilitates the use of higher fidelity methods (such as database methods, linear stability theory, or parabolized stability equations) if so desired.

I.B. RANS-based Aerodynamic Shape Optimization for NLF

Research in the area of high-fidelity aerodynamic shape optimization with laminar-turbulent transition is sparse. The majority of research in this field employs inviscid-viscous coupling strategies, making use of boundary-layer codes for the viscous formulation and either a panel method or the Euler equations for the inviscid formulation. Although the inviscid-viscous coupling strategies can be computationally cheaper than the higher-fidelity RANS solvers, the industry's trend toward the use of RANS solvers strongly suggests that NLF design tools should follow suit. Recent research making use of RANS solvers to optimize with transition prediction has shown promising results.

Driver and Zingg [17] coupled a RANS optimization framework to the MSES inviscid-viscous solver for transition prediction. This was a stop-gap approach used to successfully demonstrate the potential for NLF design using RANS-based optimization. Lee and Jameson [18] have successfully coupled a RANS

solver to a boundary-layer code and an e^N database method (making use of the Baldwin-Lomax turbulence model) for NLF design in two and three dimensions. The gradient calculations in their work did not include the transition prediction, and their optimizations focused on the elimination of shock-waves for reduced wave drag. Khayatzadeh and Nadarajah [19] successfully extended the Langtry-Menter transport equation approach to an adjoint-based optimization framework in two dimensions and applied the framework to the design of low Reynolds number NLF airfoils with separation bubbles. Design objectives investigated included the minimization of turbulent kinetic energy and the maximization of lift-to-drag ratio. More recently, several researchers have employed the Langtry-Menter approach in conjunction with costly finite-difference gradient approximations or gradient-free methods for the design of NLF airfoils and wind turbine blades [20–24]. Previous work by Rashad and Zingg also made use of a finite-difference gradient approximation [25].

The objective of this work is to advance the state-of-the-art in ASO for the NLF design of subsonic and transonic airfoils. To this end, a two-dimensional RANS solver making use of the Spalart-Allmaras turbulence model is extended to incorporate an iterative laminar-turbulent transition prediction methodology capable of accounting for the effects of Re, T_u, M, and pressure gradient (Section II). The RANS solver is subsequently employed in a sequential quadratic programming shape optimization framework making use of an augmented discrete-adjoint formulation for non-local transition criteria (Section III). Various design studies serve as a proof-of-concept for the proposed optimization framework and demonstrate the various ways in which the framework can be used to design NLF airfoils and study the various design trade-offs involved. Techniques for robust NLF design are also proposed and demonstrated.

II. Flow Solver Methodology

The steady RANS equations are solved in two dimensions using a second-order Newton-Krylov (NK) finite-difference flow solver (named Optima2D) originally developed by Nemec and Zingg [26]. The linear system that arises at each Newton iteration is solved using the preconditioned Generalized Minimum Residual (GMRES) method. Global convergence of the Newton method is made possible by an Approximate Factorization (AF) start-up algorithm. Numerical dissipation is added by either the scalar dissipation scheme of Jameson *et al.* [27] or the matrix dissipation scheme of Swanson and Turkel [28]. The turbulent eddy viscosity is computed using the one-equation Spalart-Allmaras (SA) turbulence model [29]. The remaining components of the proposed transition prediction framework include: the determination of the boundary-layer edge and properties, the calculation and evaluation of the transition criteria, and the implementation of a robust iterative procedure for transition prediction in the RANS solver.

II.A. Calculation of the Boundary-Layer Properties

By definition, the various boundary-layer properties are non-local, since they require the integration of flow quantities from the wall to the boundary-layer edge. For example, the AHD criterion requires the calculation of the displacement thickness (δ^*), momentum thickness (θ), shape-factor (H), and Pohlhausen number (Λ), all of which require the calculation of the boundary-layer thickness (δ). In this work we compute these properties making use of the available RANS solution, altogether avoiding the use of a boundary-layer solver. As such, we must somehow define the boundary-layer edge based on the RANS flow solution.

Three boundary-layer edge-finding methods have been implemented, verified and compared in the RANS flow solver, including: the compressible Bernoulli equation method [30], the Baldwin-Lomax diagnostic function method [30], and the flow vorticity and shear stress method [7]. Further implementation and verification details may be found in Rashad and Zingg [25]. The accuracy of the boundary-layer properties has also been assessed through a detailed grid convergence study and by comparison to numerical boundary-layer properties obtained from XFOIL [25]. With reasonable grid density, containing approximately 100 nodes in the boundary layer (for the scalar dissipation scheme), it was found that the boundary-layer properties can be computed directly from the RANS solution with sufficient accuracy.

II.B. Simplified e^N envelope method

The natural transition locations due to Tollmien-Schlichting instabilities are predicted using the simplified e^N envelope method developed by Drela and Giles [31] and used in both the XFOIL and MSES codes. The approach is a two-step method. First we find the critical (or neutral stability) point, that is, the point at which $Re_\theta = Re_{\theta_{\mathrm{cr}}}$. The expression for $Re_{\theta_{\mathrm{cr}}}$ is given as

$$\log_{10} Re_{\theta_{\mathrm{cr}}} = \left(\frac{1.415}{H_{\mathrm{k}}-1} - 0.489\right) \tanh\left(\frac{20}{H_{\mathrm{k}}-1} - 12.9\right) + \frac{3.295}{H_{\mathrm{k}}-1} + 0.44\,, \tag{1}$$

where the kinematic shape factor is computed based on the incompressible shape factor, H_{inc}, and the Mach number at the boundary-layer edge, M_{e}, as

$$H_{\mathrm{k}} = \frac{H_{\mathrm{inc}} - 0.290 M_{\mathrm{e}}^2}{1 + 0.113 M_{\mathrm{e}}^2}\,. \tag{2}$$

Next, we approximate the N-factor envelope by integrating the following expression in the streamwise direction, s, beginning at the critical point: [31]

$$\frac{dN}{ds} = \mathrm{fcn}(H_{\mathrm{k}}, \theta) = \frac{dN}{dRe_\theta} \cdot \frac{m+1}{2} \cdot l \cdot \frac{1}{\theta}\,, \tag{3}$$

where dN/dRe_θ, m, and l are given as follows: [31]

$$\begin{aligned}
\frac{dN}{dRe_\theta} &= 0.01\sqrt{[2.4H_\mathrm{k} - 3.7 + 2.5\tanh(1.5H_\mathrm{k} - 4.65)]^2 + 0.25} \\
m(H_\mathrm{k}) &= \left(0.058\frac{(H_\mathrm{k}-4)^2}{H_\mathrm{k}-1} - 0.068\right)\frac{1}{l(H_\mathrm{k})} \\
l(H_\mathrm{k}) &= \frac{6.54H_\mathrm{k} - 14.07}{H_\mathrm{k}^2}
\end{aligned}$$

Finally, the transition point is taken as the linearly interpolated streamwise location at which $N = N_\mathrm{crit}$, where N_crit is user-specified (typically based on experimental correlations for a given application and/or wind-tunnel).

II.C. AHD Transition Criterion

A second criterion for predicting the natural transition locations due to Tollmien-Schlichting instabilities makes use of the original work by Arnal, Habiballah, and Delcourt (AHD) [7, 14, 32]. The AHD criterion is also a two step method. First, the critical point is taken as the point at which, locally, $Re_\theta = Re_{\theta_\mathrm{cr}}$, where Re_{θ_cr} is defined as

$$Re_{\theta_\mathrm{cr}} = \exp\left[\frac{E}{H_\mathrm{inc}} - F\right]. \tag{4}$$

The transition point is then taken as the streamwise location at which $Re_\theta = Re_{\theta_\mathrm{tr}}$. This is computed by finding the intersection point of the two curves, using linear interpolation between streamwise stations. Arnal *et al.* [7] proposed the following expression for the transitional Reynolds number, Re_{θ_tr}:

$$Re_{\theta_\mathrm{tr}} = Re_{\theta_\mathrm{cr}} + A\cdot\exp(B\cdot\overline{\Lambda_2})\left[\ln(C\cdot T_\mathrm{u}) - D\cdot\overline{\Lambda_2}\right], \tag{5}$$

where T_u is the freestream turbulence level, $\overline{\Lambda_2}$ is the mean Pohlhausen parameter given as

$$\Lambda_2 = \frac{\theta^2}{\nu}\frac{dU_\mathrm{e}}{ds} \quad\Longrightarrow\quad \overline{\Lambda_2} = \frac{1}{s - s_\mathrm{cr}}\int_{s_\mathrm{cr}}^{s}\Lambda_2 ds\,, \tag{6}$$

and the functions A through F are computed as a function of the Mach number at the boundary-layer edge, M_e, as follows: [32]

$$
\begin{aligned}
A &= 98.64M_e^3 - 356.44M_e^2 + 117.13M_e - 236.69 \\
B &= -13.04M_e^4 + 38.5M_e^3 - 30.07M_e^2 + 10.89M_e + 22.7 \\
C &= 0.21M_e^3 + 4.79M_e^2 - 1.76M_e + 22.56 \\
D &= -3.48M_e^4 + 6.26M_e^3 - 3.45M_e^2 + 0.23M_e + 12 \\
E &= 0.6711M_e^3 - 0.7379M_e^2 + 0.167M_e + 51.904 \\
F &= 0.3016M_e^5 - 0.7061M_e^4 + 0.3232M_e^3 - 0.0083M_e^2 \\
&\quad -0.1745M_e + 14.6 \, .
\end{aligned}
$$

II.D. RANS Implementation

II.D.1. Iterative Transition Prediction Procedure

Automatic transition prediction in the RANS solver is achieved through an iterative process. Variations of this procedure have been developed and employed by Brodeur and van Dam [33], Krumbein [34], Cliquet *et al.* [7], and Mayda [35]. The present implementation borrows ideas from all of the above, particularly that of Krumbein.

The incorporation of free transition into the implicit solver and convergence to steady-state is achieved in the following three phases:

1. Start-up from freestream conditions with fixed transition locations (AF solver).

2. Convergence with free transition-point movement (AF solver).

3. Convergence with the final fixed transition locations (NK solver).

In the first phase, an initial guess of the transition locations (top and bottom surfaces) is required and typically taken at 25% chord. Transition is then fixed to occur at the initial locations using the transition region model, as described in the next section. When the L_2-norm of the flow residual has been reduced to 5×10^{-6}, the second phase begins. Note that the tight tolerance during the start-up phase was chosen to ensure sufficiently accurate boundary-layer properties for transition prediction, which, in turn, requires that any oscillations in the density, pressure and velocities have been sufficiently damped [36].

When the second phase begins, the transition prediction module is invoked to determine the new transition locations. This step includes the determination of the boundary-layer edge, the calculation of the laminar boundary-layer properties, and the evaluation of a transition prediction criterion. The forced transition points are then moved upstream or downstream as required toward the newly predicted transition points. Note

that in order to predict transition downstream of a forced transition location, the boundary-layer properties must be extrapolated into the turbulent region, which is performed using a linear extrapolation [35]. The transition point movement is under-relaxed, such that

$$X_{\mathrm{f}}^{\mathrm{new}} = \min\left(\Delta X_{\max}\,,\; X_{\mathrm{f}}^{\mathrm{old}} - \omega\left(X_{\mathrm{f}}^{\mathrm{old}} - X_{\mathrm{p}}\right)\right)\,, \tag{7}$$

where ω is the under-relaxation factor, X_{f} and X_{p} represent the normalized chord locations of the forced and predicted transition points, respectively, and the min function limits the transition point movement at any given update. This limit on the transition point movement is selected as $\Delta X_{\max} = 0.2$ for $M_\infty < 0.65$ and $\Delta X_{\max} = 0.05$ for $M_\infty \geq 0.65$, which helps to avoid shock-induced separation when shockwaves are present during free transition point movement. When the L_2-norm of the flow residual returns to a magnitude of 5×10^{-6}, the predicted and forced transition points are again updated. The iterative transition prediction procedure is considered converged when the absolute value of the *transition residual*, given as $|\boldsymbol{\mathcal{R}}_{\mathrm{tr}}| = |X_{\mathrm{f}} - X_{\mathrm{p}}|$, has converged to a tolerance of ϵ_{tp}. From numerical experimentation over a eide range of flight conditions, an under-relaxation factor of $\omega = 0.9$ has been selected as a good compromise between efficiency and robustness. When the transition prediction procedure has converged, the third and final phase begins.

In the third phase, with X_{f} equal to X_{p}, the flow solver switches from the AF algorithm to the NK algorithm. The solver then continues to converge until the magnitude of the flow residual has reduced to a tolerance of ϵ_{nk}. For the purposes of gradient-based aerodynamic shape optimization, ϵ_{tp} and ϵ_{nk} are set to 10^{-8} and 10^{-11}, respectively, ensuring a sufficiently smooth design space for optimization.

II.D.2. Modelling of Transitional Flow Regions

The transition to turbulence is enforced in the Navier-Stokes solution by one of two methods. The first makes use of the trip term and the f_{t_1} and f_{t_2} trip functions in the SA model, as published by Spalart and Allmaras [29].

The second transition region model considered makes use of a streamwise varying intermittency function. Following the work of Cliquet *et al.* [7], the intermittency function, γ, scales the turbulent eddy-viscosity directly from the SA model (or any other eddy-viscosity model) such that

$$\mu_{\mathrm{tr}} = \max(\,\gamma\mu_{\mathrm{t}}\,,\,\mu_{\mathrm{t}_\infty}\,)\,, \quad \text{where} \quad 0 \leq \gamma \leq 1\,. \tag{8}$$

The max function in (8) ensures that the scaled eddy-viscosity, μ_{tr}, does not take on values less than the freestream value in the laminar regions.

In this work, a new form of the streamwise intermittency function has been designed based on a different

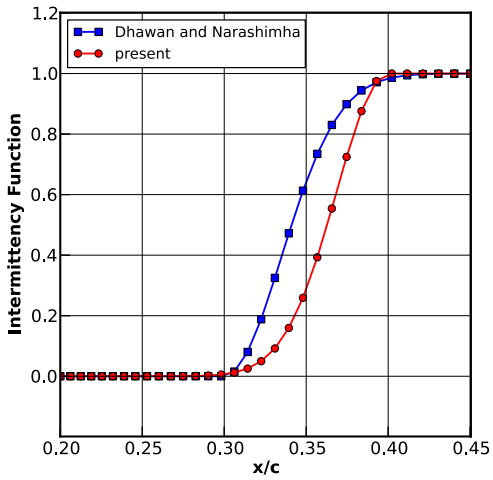

Figure 1. Intermittency distributions with $x_{\rm tr}=0.3$ and $l_{\rm tr}=0.10$

function developed by Dhawan and Narasimha [37]. The new form of the S-shaped function is computed as a function of the local chord position, x, the specified transition point, $x_{\rm tr}$, and the specified transition length, $l_{\rm tr}$ as

$$\gamma(x, x_{\rm tr}, l_{\rm tr}) = \exp(-5\,\xi^2)\,, \quad \text{where} \quad \xi = 1 + \frac{x_{\rm tr} - x}{l_{\rm tr}}\,, \tag{9}$$

whereas Dhawan and Narashimha's original intermittency function takes the form

$$\gamma(x, x_{\rm tr}, l_{\rm tr}) = 1 - \exp(0.412\,\zeta^2)\,, \quad \text{where} \quad \zeta = 3.36\,\frac{x - x_{\rm tr}}{l_{\rm tr}}\,. \tag{10}$$

Figure 1 provides a plot of the intermittency distributions with a specified transition location at 30% chord and a specified transition length of 10%. By design, the intermittency functions asymptote to a value of zero in the fully laminar region and to unity in the fully turbulent region. The present form of the intermittency given by (9) is designed to introduce a more gradual initial ramp-up of the eddy-viscosity, and is very close to a horizontally mirrored image of (10). The importance of the smooth (more gradual) initial ramp-up is two-fold. First, it helps to avoid oscillations that can appear in the flow variables just upstream of the transition point due to an abrupt increase in $\mu_{\rm tr}$. These oscillations are often observed in the pressure and skin friction profiles and sometimes lead to unphysical or unresolved flow separation (negative skin friction coefficients at a single node) on the airfoil. Second, the smooth ramp-up ensures a sufficiently smooth design space as required for gradient-based optimization.

A comparison of the eddy viscosity ramp-up using the intermittency function as compared to the Spalart-Allmaras trip terms may be found in Rashad and Zingg [25]. It was observed that the Spalart-Allmaras trip terms result in sharp increase in the eddy viscosity in the boundary layer, in comparison to the much smoother introduction of eddy viscosity given by the intermittency functions. The sharp increase in the eddy

viscosity observed when using the SA trip term was found to cause locally non-smooth design spaces for the grids typically employed for transition prediction [25]. Furthermore, the intermittency transition region model is particularly easy to implement since the only modification necessary is to replace the variable μ_t with its scaled equivalent, μ_{tr}, everywhere that it appears in the mean-flow RANS equations. Note that it is not necessary to modify the turbulence model explicitly in any way, instead the solution to $\tilde{\nu}$ implicitly accounts for the intermittency scaling through its coupling to the mean-flow variables as convergence to steady-state is achieved.

III. Optimization Framework

The goal of the aerodynamic shape optimization framework is to minimize the specified design objective, J, with respect to the design variables, X, subject to linear and nonlinear constraints. Although the optimizer can handle several different design objectives, in this work the focus is on lift-constrained drag minimization. The proposed optimization framework consists of the following: (i) a two-dimensional RANS flow solver (described in the preceding section), (ii) a geometry parametrization and mesh movement algorithm, (iii) a sequential quadratic programming algorithm, and (iv) a discrete-adjoint gradient computation.

The airfoil geometry is parametrized using B-splines, the details of which may be found in Nemec and Zingg [26]. The design variables, X, are defined as the y-coordinates of the B-spline control points; the control points are free to move in the vertical direction to facilitate shape changes during the optimization cycle. The angle of attack of the airfoil is an additional design variable. The algebraic grid-perturbation strategy described in Nemec and Zingg [26] is used to ensure that the computational grid is smoothly adjusted to conform to the changing geometric configurations.

The SNOPT general purpose Sequential Quadratic Programming (SQP) algorithm [38] is employed as the optimizer in this work. SNOPT requires the gradients of the objective function and constraints; ensuring sufficiently accurate gradients is of paramount importance to the success of the SQP algorithm. Three methods for computing accurate gradients (that incorporate the sensitivities of the transition criterion) have been implemented, including a parallelized finite-difference gradient evaluation [25], the direct (or flow-sensitivity) method, and the discrete-adjoint gradient method, presented in the next section.

III.A. Discrete-Adjoint Gradient Evaluation

The principal advantage of the adjoint method is that its cost does not scale with the number of design variables, but rather with the number of objectives and nonlinear constraints [39]. Hence, the objective function gradient evaluation only requires one flow solution and one adjoint solution; for lift-constrained drag minimizations, an additional adjoint solution is required for the gradient of the lift constraint.

In the discrete-adjoint approach, the gradient is evaluated using the following expression [26]:

$$G = \frac{dJ}{dX} = \frac{\partial J}{\partial X} - \psi^T \frac{\partial R}{\partial X} \,, \tag{11}$$

where $R = R[X, Q(X)]$ represents the discretized RANS residual vector. The vectors $\frac{\partial J}{\partial X}$ and $\frac{\partial R}{\partial X}$ are obtained by a centered-difference approximation, which does not require any additional flow solutions and is computationally inexpensive. The vector of adjoint variables, ψ, is obtained by solving the linear system of equations given by

$$\frac{\partial R}{\partial Q}^T \psi = \frac{\partial J}{\partial Q}^T \,, \tag{12}$$

where Q is the vector of conserved flow variables.

III.B. Augmented Adjoint Formulation for Transition Prediction

The e^N and AHD transition criteria (described in Sections II.B and II.C, respectively) are non-local in their formulation in that they use flow variables in their evaluation belonging to grid points which are not physically near the transition point. As such, special consideration must be taken when evaluating and deriving an adjoint formulation capable of incorporating their sensitivities, particularly when trying to preserve the sparsity pattern of the flow Jacobian matrix. The proposed approach is to append a new adjoint vector, $\boldsymbol{\psi}_{\mathrm{tr}}$, to the original adjoint vector, such that $\overline{\psi} \Rightarrow [\psi \,;\, \boldsymbol{\psi}_{\mathrm{tr}}]$. Henceforth, the overbar shall be used to indicate an augmented vector. The length of $\boldsymbol{\psi}_{\mathrm{tr}}$ corresponds to the number of transition points, N_{tr}, which is equal to two for a single-element airfoil. For 3D wing configurations, the transition lines may be defined by a spanwise distribution of transition points [40]; the total number of spanwise transition points on all surfaces gives N_{tr}.

To compute the new adjoint variables, we specify a corresponding number of new residual equations, such that $\overline{\boldsymbol{\mathcal{R}}} \Rightarrow [\boldsymbol{\mathcal{R}} \,;\, \boldsymbol{\mathcal{R}}_{\mathrm{tr}}]$. The new transition residual equations represent the distance between the forced and predicted transition locations, $\boldsymbol{\mathcal{R}}_{\mathrm{tr}} = \mathbf{X}_{\mathrm{f}} - \mathbf{X}_{\mathrm{p}}$, as described in Section II.D.1. The transition residual vector is satisfied ($\boldsymbol{\mathcal{R}}_{\mathrm{tr}} = 0$) when the forced transition points are in locations consistent with the given transition criterion ($\mathbf{X}_{\mathrm{f}} = \mathbf{X}_{\mathrm{p}}$).

In addition, the vector of conserved flow variables must be augmented to include the forced transition locations, such that $\overline{\mathbf{Q}} \Rightarrow [\mathbf{Q} \,;\, \mathbf{X}_{\mathrm{f}}]$. The entire adjoint vector, $\overline{\boldsymbol{\psi}}$, is computed by solving the augmented linear system of equations given by

$$\frac{\partial \overline{R}}{\partial \overline{Q}}^T \overline{\psi} = \frac{\partial J}{\partial \overline{Q}}^T \tag{13}$$

$$\downarrow$$

$$\left[\begin{array}{c:c} \frac{\partial R}{\partial Q} & \frac{\partial R}{\partial X_\mathrm{f}} \\ \hdashline \frac{\partial R_\mathrm{tr}}{\partial Q} & \frac{\partial R_\mathrm{tr}}{\partial X_\mathrm{f}} \end{array}\right]^T \left[\begin{array}{c} \psi \\ \hdashline \boldsymbol{\psi}_\mathrm{tr} \end{array}\right] = \left[\begin{array}{c} \frac{\partial J}{\partial Q} \\ \hdashline \frac{\partial J}{\partial X_\mathrm{f}} \end{array}\right]^T .$$

The $\frac{\partial R}{\partial X_\mathrm{f}}$ matrix represents the sensitivity of the flow residual to the forced transition points. It is computed efficiently using a centered difference approximation requiring only two evaluations of the flow residual for each transition point. The matrix $\frac{\partial R_\mathrm{tr}}{\partial X_\mathrm{f}}$ represents the sensitivity of the transition residual to the forced transition points, which by the definition of $R_\mathrm{tr} = X_\mathrm{f} - X_\mathrm{p}$, is simply the $N_\mathrm{tr} \times N_\mathrm{tr}$ identity matrix. Furthermore, the vector $\frac{\partial J}{\partial X_\mathrm{f}}$ is simply the null vector for typical objectives and constraints such as lift and drag, since these objectives do not depend explicitly (but rather implicitly) on the transition points. The matrix $\frac{\partial R_\mathrm{tr}}{\partial Q}$ is by far the most complex of the new matrices in the augmented formulation, as it represents the sensitivity of the transition residual (including the evaluation of the boundary-layer edge, the boundary-layer properties, and the given transition criterion) to the conserved flow variables. This matrix is computed accurately using a complex-step approximation [41] discussed further below.

The proposed approach has several advantages. First and foremost, the sensitivities of the given transition criterion with respect to the design variables are explicitly incorporated into the adjoint gradient, in turn allowing the optimizer to exploit that information. Second, the non-locality in the given transition criterion is confined to the last N_tr rows of the new Jacobian matrix, $\frac{\partial \overline{R}}{\partial \overline{Q}}$. Note that the new adjoint system is only slightly larger than the original system, since the number of additional rows in the new Jacobian is only N_tr. Thus, the use of the complex-step approximation in the calculation of $\frac{\partial R_\mathrm{tr}}{\partial Q}$ does not incur significant additional expense. Furthermore, the specific nodes involved in satisfying the transition criteria (i.e. from the critical point to the transition point, and from the airfoil surface to the boundary-layer edge) are known; thus, only that subset of nodes is perturbed when using the complex-step approximation to evaluate $\frac{\partial R_\mathrm{tr}}{\partial Q}$.

Third, no extra work is needed to incorporate the sensitivities of a new or different user-specified transition criterion. Fourth, the iterative procedure used to determine the final forced transition locations, as described in Section II.D, need not be explicitly included, since the converged RANS solution satisfies the transition criterion, $R_{\text{tr}} = 0$, and the sensitivities of the given transition criterion are included by the addition of the new adjoint variables. Finally, the sensitivities of R and J with respect to X_{f} (that is, $\frac{\partial J}{\partial X_{\text{f}}}$ and $\frac{\partial R}{\partial X_{\text{f}}}$) need not contain any information about the transition criterion.

Two solution strategies have been developed to solve the augmented system. Upon solving for $\overline{\psi}$, the gradient components may be computed by the augmented version of (11) given by

$$G_i = \frac{d\mathcal{J}}{dx_i} = \frac{\partial \mathcal{J}}{\partial x_i} - \overline{\boldsymbol{\psi}}^T \frac{\partial \overline{\boldsymbol{\mathcal{R}}}}{\partial x_i} \qquad \text{for} \quad i = 1 \ldots N_{\text{D}} \,, \tag{14}$$

where N_{D} is the number of design variables, and the last N_{tr} entries of $\frac{\partial \overline{\boldsymbol{\mathcal{R}}}}{\partial x_i}$ are given by the differentiation of the transition residual with respect to the design variables, that is, $\frac{\partial \boldsymbol{\mathcal{R}}_{\text{tr}}}{\partial x_i}$. Keeping $\overline{\mathbf{Q}}$ constant, this differentiation is cheaply and accurately computed by a centered-difference approximation.

III.C. Solving the Augmented Adjoint System

III.C.1. Iterative Solution Strategy

An iterative approach was first developed to solve the augmented adjoint system by making multiple calls to the GMRES solver. Details of the solution procedure may be found in Rashad and Zingg [42], which includes a study of the convergence and accuracy of the procedure.

While the iterative solution strategy provides accurate gradient vectors (see Section IV.B), the gradient computation unfortunately requires upwards of 10-20 major iterations to converge, each one requiring approximately 200 minor GMRES iterations. As an example, Figure 2 presents a typical convergence history of the iterative solution strategy; further discussion may be found in Rashad and Zingg [42]. This is in contrast to a single call to GMRES (i.e. one major iteration) required for the original fully-turbulent (or fixed-transition) adjoint system given by (12). Furthermore, for lift-constrained drag minimization, two adjoint gradients are required, and thus, the GMRES solver will be invoked upwards of 20-40 times for the convergence of two augmented systems. This motivates the development of a more efficient solution strategy for the augmented system, presented in the next section.

III.C.2. Non-Iterative Solution Strategy

A more efficient solution strategy is possible by solving three intermediate problems defined by making some strategic substitutions prior to directly computing ψ and ψ_{tr}. This approach requires only three calls to the

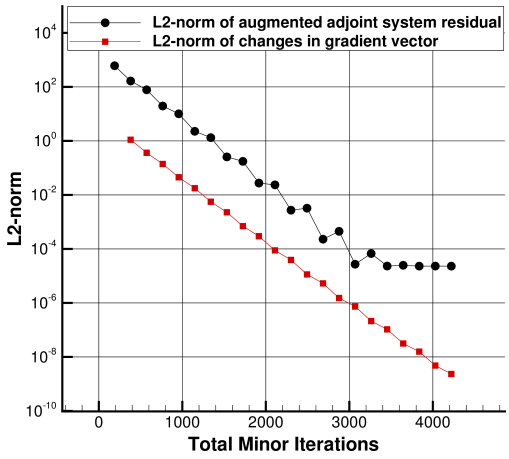

Figure 2. Iterative solution strategy: convergence of augmented adjoint system

preconditioned GMRES solver, in contrast to 10-20 calls required for the iterative solution strategy.

We begin by writing the augmented system of equations (13) as follows:

$$\frac{\partial \boldsymbol{\mathcal{R}}}{\partial \mathbf{Q}}^T \boldsymbol{\psi} + \frac{\partial \boldsymbol{\mathcal{R}}_{\mathrm{tr}}}{\partial \mathbf{Q}}^T \boldsymbol{\psi}_{\mathrm{tr}} = \frac{\partial \mathcal{J}}{\partial \mathbf{Q}}^T , \tag{15}$$

$$\frac{\partial \boldsymbol{\mathcal{R}}}{\partial \mathbf{X}_{\mathrm{f}}}^T \boldsymbol{\psi} + \frac{\partial \boldsymbol{\mathcal{R}}_{\mathrm{tr}}}{\partial \mathbf{X}_{\mathrm{f}}}^T \boldsymbol{\psi}_{\mathrm{tr}} = \frac{\partial \mathcal{J}}{\partial \mathbf{X}_{\mathrm{f}}}^T . \tag{16}$$

Let us now write the identity matrix as the product of the Jacobian-transposed with its own inverse, that is,

$$\mathcal{I} = \frac{\partial \boldsymbol{\mathcal{R}}}{\partial \mathbf{Q}}^T \left(\frac{\partial \boldsymbol{\mathcal{R}}}{\partial \mathbf{Q}}^T \right)^{-1} \tag{17}$$

By pre-multiplying the second term on the left-hand side of (15) by (17) we have

$$\frac{\partial \boldsymbol{\mathcal{R}}}{\partial \mathbf{Q}}^T \boldsymbol{\psi} + \frac{\partial \boldsymbol{\mathcal{R}}}{\partial \mathbf{Q}}^T \left(\frac{\partial \boldsymbol{\mathcal{R}}}{\partial \mathbf{Q}}^T \right)^{-1} \frac{\partial \boldsymbol{\mathcal{R}}_{\mathrm{tr}}}{\partial \mathbf{Q}}^T \boldsymbol{\psi}_{\mathrm{tr}} = \frac{\partial \mathcal{J}}{\partial \mathbf{Q}}^T \tag{18}$$

From the quadruple-product term in (18), we can define an intermediate matrix, $M \in \mathbb{R}^{N_{\mathrm{q}} \times N_{\mathrm{tr}}}$, as

$$M = \left(\frac{\partial \boldsymbol{\mathcal{R}}}{\partial \mathbf{Q}}^T \right)^{-1} \frac{\partial \boldsymbol{\mathcal{R}}_{\mathrm{tr}}}{\partial \mathbf{Q}}^T . \tag{19}$$

Solving for the two columns that make up M (since $N_{\mathrm{tr}} = 2$) defines the first two intermediate problems that must be solved. To define the third intermediate problem we first substitute the matrix M into (18) and rearrange to get

$$\frac{\partial \boldsymbol{\mathcal{R}}}{\partial \mathbf{Q}}^T (\boldsymbol{\psi} + M \boldsymbol{\psi}_{\mathrm{tr}}) = \frac{\partial \mathcal{J}}{\partial \mathbf{Q}}^T . \tag{20}$$

Next we define a new vector, $\widetilde{\boldsymbol{\psi}} \in \mathbb{R}^{N_{\mathrm{q}}}$, as

$$\widetilde{\boldsymbol{\psi}} = \boldsymbol{\psi} + M\boldsymbol{\psi}_{\mathrm{tr}}\,, \tag{21}$$

and substitute it into (20) to get a system of equations of the form

$$\frac{\partial \boldsymbol{\mathcal{R}}}{\partial \mathbf{Q}}^T \widetilde{\boldsymbol{\psi}} = \frac{\partial \mathcal{J}}{\partial \mathbf{Q}}^T . \tag{22}$$

Solving for $\widetilde{\boldsymbol{\psi}}$ represents the third and final intermediate problem. Note that the large, sparse system of equations given by (22) is identical to the original adjoint system (12) without any augmentation.

To solve for the matrix M we first rewrite (19) as follows:

$$\frac{\partial \boldsymbol{\mathcal{R}}}{\partial \mathbf{Q}}^T M = \frac{\partial \boldsymbol{\mathcal{R}}_{\mathrm{tr}}}{\partial \mathbf{Q}}^T . \tag{23}$$

Letting the subscripts 1 and 2 denote the first and second columns of both M and $\frac{\partial \boldsymbol{\mathcal{R}}_{\mathrm{tr}}}{\partial \mathbf{Q}}^T$, we can then solve the following systems of equations for each column of M independently:

$$\frac{\partial \boldsymbol{\mathcal{R}}}{\partial \mathbf{Q}}^T M_1 = \left(\frac{\partial \boldsymbol{\mathcal{R}}_{\mathrm{tr}}}{\partial \mathbf{Q}}^T\right)_1 , \tag{24}$$

$$\frac{\partial \boldsymbol{\mathcal{R}}}{\partial \mathbf{Q}}^T M_2 = \left(\frac{\partial \boldsymbol{\mathcal{R}}_{\mathrm{tr}}}{\partial \mathbf{Q}}^T\right)_2 . \tag{25}$$

Since (23), (24), and (25) all share the same Jacobian matrix on the left-hand side, we can solve each system using the same preconditioned GMRES approach previously discussed.

All that remains is to solve for $\boldsymbol{\psi}$ and $\boldsymbol{\psi}_{\mathrm{tr}}$. From (21) we have

$$\boldsymbol{\psi} = \widetilde{\boldsymbol{\psi}} - M\boldsymbol{\psi}_{\mathrm{tr}}\,, \tag{26}$$

and substituting this expression into (16) we have

$$\frac{\partial \boldsymbol{\mathcal{R}}}{\partial \mathbf{X}_{\mathrm{f}}}^T \left(\widetilde{\boldsymbol{\psi}} - M\boldsymbol{\psi}_{\mathrm{tr}}\right) + \frac{\partial \boldsymbol{\mathcal{R}}_{\mathrm{tr}}}{\partial \mathbf{X}_{\mathrm{f}}}^T \boldsymbol{\psi}_{\mathrm{tr}} = \frac{\partial \mathcal{J}}{\partial \mathbf{X}_{\mathrm{f}}}^T . \tag{27}$$

Having previously solved for $\widetilde{\boldsymbol{\psi}}$ and M, we can solve for $\boldsymbol{\psi}_{\mathrm{tr}}$ directly (using Cramer's rule, for example) by rearranging (27) to get the following system of equations (which is of length $N_{\mathrm{tr}} = 2$):

$$\left(\frac{\partial \boldsymbol{\mathcal{R}}_{\mathrm{tr}}}{\partial \mathbf{X}_{\mathrm{f}}}^T - \frac{\partial \boldsymbol{\mathcal{R}}}{\partial \mathbf{X}_{\mathrm{f}}}^T M\right) \boldsymbol{\psi}_{\mathrm{tr}} = \frac{\partial \mathcal{J}}{\partial \mathbf{X}_{\mathrm{f}}}^T - \frac{\partial \boldsymbol{\mathcal{R}}}{\partial \mathbf{X}_{\mathrm{f}}}^T \widetilde{\boldsymbol{\psi}}\,. \tag{28}$$

Note that since $\frac{\partial \boldsymbol{\mathcal{R}}_{\text{tr}}}{\partial \mathbf{X}_{\text{f}}}$ is the identity matrix and $\frac{\partial \mathcal{J}}{\partial \mathbf{X}_{\text{f}}}$ is the null vector, (28) simplifies to

$$\left(\mathcal{I} - \frac{\partial \boldsymbol{\mathcal{R}}}{\partial \mathbf{X}_{\text{f}}}^{T} M \right) \boldsymbol{\psi}_{\text{tr}} = -\frac{\partial \boldsymbol{\mathcal{R}}}{\partial \mathbf{X}_{\text{f}}}^{T} \widetilde{\boldsymbol{\psi}} \,. \tag{29}$$

Finally, the vector $\boldsymbol{\psi}$ can be solved for directly from (26).

To summarize, the following five steps are performed to solve the augmented adjoint system:

1. Use preconditioned GMRES to solve (23) for $\widetilde{\boldsymbol{\psi}}$.
2. Use preconditioned GMRES to solve (24) for M_1.
3. Use preconditioned GMRES to solve (25) for M_2.
4. Solve (29) directly for $\boldsymbol{\psi}_{\text{tr}}$.
5. Solve (26) directly for $\boldsymbol{\psi}$.

It is important to note that if the optimization problem requires any additional adjoint gradient computations for any nonlinear constraints (such as lift and/or moment constraints), it is not necessary to repeat steps 2 and 3 since they are based solely on the left-hand side matrix of the augmented system, which does not depend on the objective or constraints under consideration.

The non-iterative solution strategy has several key advantages over the iterative solution strategy discussed in the previous section. First, it does away with the issues surrounding an iterative procedure, including the need for an initial guess on $\boldsymbol{\psi}_{\text{tr}}$, convergence criteria, and the studies required for convergence acceleration and robustness. Furthermore, the accuracy of the resulting gradient vectors do not depend in any way on the convergence of the major iterations that exist for the iterative approach. Perhaps most important from a practical standpoint, the computational cost of the non-iterative strategy is many times smaller than the iterative approach. The computational cost of the various gradient evaluation techniques will be quantified and compared in Section IV.B. For a single adjoint gradient, the non-iterative method requires only three calls to GMRES rather than 10-20 calls. For a lift-constrained drag minimization, the cost benefits are even greater, requiring a total of only four calls to GMRES rather than 20-40 calls. As a result of these advantages, the non-iterative method is selected as the solution strategy for the augmented adjoint system.

III.D. Multipoint Optimization

We use multipoint optimization to ensure that our aerodynamic designs perform reasonably well over a given flight envelope. This is particularly important in the design of NLF airfoils, which, in order to maximize the extent of laminar flow, tend to take the boundary-layer very close to the point of separation prior to pressure recovery. As such, the off-design performance of NLF airfoils must be considered during the design process to ensure practical and robust designs. We use the methodology of Buckley and Zingg [43] to perform multipoint optimization capable of handling a comprehensive set of aerodynamic design requirements. In particular, we are interested in considering a range of Reynolds numbers, Mach numbers, and aircraft weights (W). We keep the cruise altitude constant in this work (however it can also be included) and by specifying a range of Mach numbers and aircraft weights, we can obtain the corresponding range of Reynolds numbers and lift requirements. The optimizer then minimizes the weighted integral of the objective (in our case, the drag coefficient) subject to the lift constraints (one for each design point). Also note that each operating point has an associated angle of attack, all of which are included as additional design variables. The weighted integral is defined as [43]

$$\int_{W_1}^{W_2}\int_{M_1}^{M_2} C_d\left(M,W\right)\mathcal{Z}\left(M,W\right)dMdW \tag{30}$$

where $\mathcal{Z}$ is a weighting function to be specified by the designer. This weighting function allows the designer to specify the importance of each design point according to their own priorities. The objective function, J, is an approximation to (30) given by

$$\mathcal{J} = \sum_{i=1}^{N_W}\sum_{j=1}^{N_M} \mathcal{T}_{i,j}\, C_d\left(M_i,W_j\right)\mathcal{Z}\left(M_i,W_j\right)\Delta M\Delta W\,, \tag{31}$$

where N_M and N_W are the numbers of quadrature points, and ΔM and ΔW are the corresponding spacings between quadrature points. The $\mathcal{T}_{i,j}$ are the associated quadrature weights used to approximate the integral. In this work, the trapezoidal quadrature rule is employed.

The above multipoint formulation requires one flow solution and two adjoint solutions for each operating point. Buckley and Zingg [43] have parallelized the multipoint framework such that multiple processors compute the necessary objective, constraint, and gradient information. This approach has been shown to be an effective technique for robust and efficient aerodynamic design over a range of operating conditions [43]. Full details of the various operating conditions and their associated weights are presented in Section IX.

IV. Verification and Validation

IV.A. Transition Prediction

IV.A.1. NLF-0416 Airfoil

The transition prediction capabilities of the flow solver are validated by comparison to experimental transition data for the NLF-0416 airfoil developed by Somers [44]. The experimental results for NLF-0416 were obtained in the Langley Low Turbulence Pressure Tunnel (LTPT) using microphoned pressure taps [44]. The resolution of the experiments corresponds to the physical spacing of the microphoned taps along the chord of the airfoil.

The test case results are for a 575×224 C-grid around the NLF-0416 airfoil at $Re = 4 \times 10^6$, $M = 0.2$, and $T_u = 0.1\%$ (and $N = 8$ for XFOIL). The transition points predicted by both Optima2D and XFOIL are presented in Figure 3, along with the wind tunnel experimental data. The results of this test case show that the predictive capabilities of Optima2D match closely with the published experimental results over a range of lift coefficients. Figure 3(c) presents the drag polar for the NLF-0416 airfoil using both Optima2D and XFOIL. Good agreement is observed between the experimental results and the predicted transition locations and drag polar computed using Optima2D. In Somers' report [44], the freestream turbulence intensity, T_u, was unfortunately not published for the NLF-0416 experiments. It is possible that the wind tunnel may have had lower or higher T_u than the 0.1% used for the computations. Further verification and validation results may be found in Rashad and Zingg [25].

IV.B. Accuracy and Efficiency of Gradient Computations

IV.B.1. Accuracy of Gradient Computations

To verify the accuracy of the gradient evaluation and, in particular, the augmented adjoint formulation for transition prediction (as presented in Sections III.B and III.C) we compare the gradient vectors obtained using the following evaluation techniques (with the following labels):

- **Finite-difference gradient method (FD):** Computes a centered-difference approximation of the gradient vector, as

$$\frac{d\mathcal{J}}{dx_i} = \frac{J(\mathbf{x}+h\boldsymbol{e}_i, Q(\mathbf{x}+h\boldsymbol{e}_i)) - J(\mathbf{x}-h\boldsymbol{e}_i, Q(\mathbf{x}-h\boldsymbol{e}_i))}{2h} \quad \text{for} \quad i = 1 \ldots N_{\mathrm{D}} \tag{32}$$

  where $\boldsymbol{e}_i$ is the i^{th} unit vector, and h is the step-size defined below.

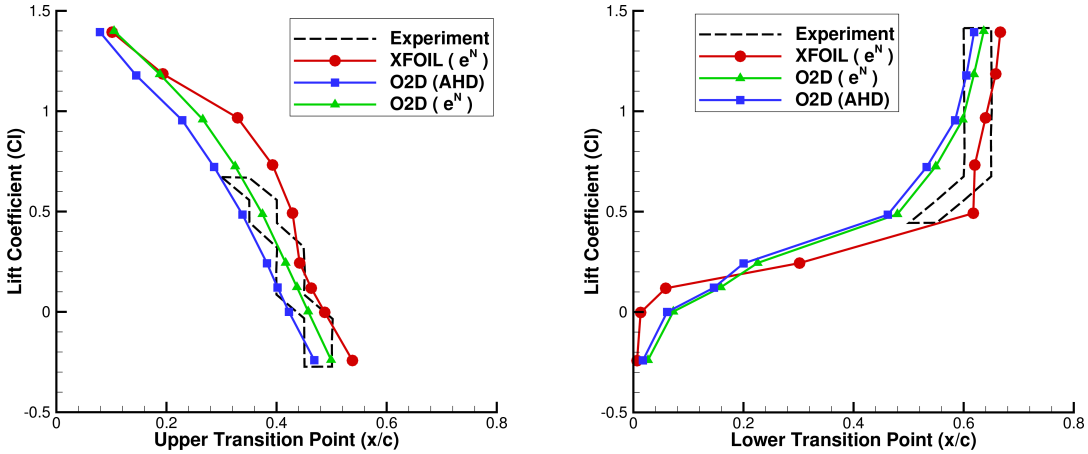

(a) Upper surface transition prediction results

(b) Lower surface transition prediction results

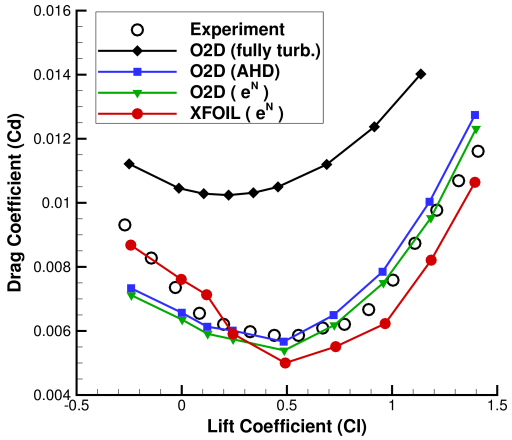

(c) Comparison of drag polars

Figure 3. NLF-0416 transition prediction validation

- **Flow (or direct) sensitivity method (SN):** Computes the gradient vector by solving

$$\frac{d\mathcal{J}}{dx_i} = \frac{\partial \mathcal{J}}{\partial x_i} + \frac{\partial \mathcal{J}}{\partial \mathbf{Q}} \frac{\partial \mathbf{Q}}{\partial x_i} \qquad \text{for} \quad i = 1 \ldots N_{\mathrm{D}} \,, \tag{33}$$

making use of the same augmented Jacobian matrix as used in the discrete-adjoint formulation. Indeed, an analogous iterative solution procedure to that described in Section III.C.1 is employed to solve

$$\frac{\partial \boldsymbol{\mathcal{R}}}{\partial \mathbf{Q}} \frac{\partial \mathbf{Q}}{\partial x_i} = -\frac{\partial \boldsymbol{\mathcal{R}}}{\partial x_i} \qquad \text{for} \quad i = 1 \ldots N_{\mathrm{D}} \,. \tag{34}$$

- **Iterative augmented adjoint method (*iAD*):** Solves (13) making use of the iterative solution strategy described in III.C.1.

- **Non-iterative augmented adjoint method (*nAD*):** Solves (13) making use of the non-iterative solution strategy described in III.C.2

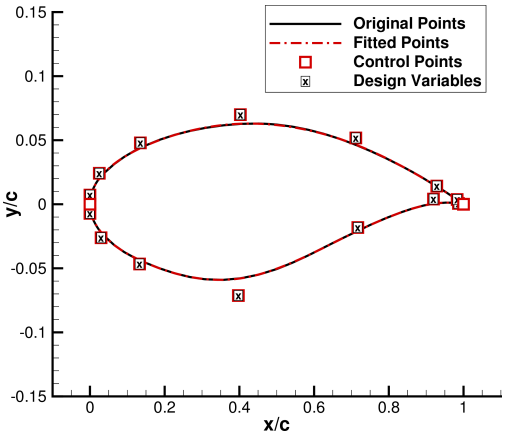

Figure 4. RAE-2822 B-spline parameterization

The accuracy assessment is carried out by performing a single iteration of the optimization, using each of the above listed gradient evaluation techniques. As shown in Figure 4, the RAE-2822 airfoil geometry is parameterized by seventeen B-spline control points, fourteen of which are selected as the design variables in addition to the angle of attack. The flight conditions are $Re = 15.7 \times 10^6$, $M = 0.6$, $AoA = 1°$, and the e^N transition prediction criterion is employed with $N_{\text{crit}} = 9$. A step-size of 1×10^{-6} is used for the finite-difference gradient, resulting from a step-size study. Table 1 compares the resulting objective function gradients. The first 14 components are the geometric design variables, the last is the angle of attack (AoA). The results demonstrate excellent agreement between all methods for computing the gradient vector. The percent difference between the FD and nAD gradients is less than 1% for all components. Similar results were observed for the lift-constraint gradient. Since the finite-difference method does not require differentiating the code, it serves to verify that the differentiation was performed accurately in the remaining gradient evaluation techniques. The augmented Jacobian matrix is also verified by the excellent agreement found between the flow sensitivity and adjoint gradient results; these methods employ the same augmented Jacobian matrix, but use entirely different approaches for computing the gradient.

IV.B.2. Comparison of Computational Cost

The computational cost of each gradient evaluation technique is now compared. For 15 design variables, a centered-difference approximation requires 30 flow solutions, the flow sensitivity method requires 15 solutions to the augmented flow sensitivity system given by (34), and the discrete-adjoint method requires one solution to the augmented adjoint system given by (13). Table 2 provides the computational cost in terms of total wall-clock time to compute the gradient for a single optimization iteration. It also compares the cost of computing an additional gradient vector associated with the lift-constraint gradient, since both gradient vectors are required for the lift-constrained drag minimizations presented in the next chapter.

Table 1. Comparison of objective function gradient components computed using various gradient evaluation techniques: RAE-2822, $Re = 15.7\times10^6$, $M = 0.6$, $AoA = 1^\circ$

Design	nAD	FD$-n$AD		SN$-n$AD		iAD$-n$AD	
Variable	Gradient	Diff.	% Diff.	Diff.	% Diff.	Diff.	% Diff.
1	0.0702067611	-2.2821E-06	-3.2506E-03	1.1238E-11	1.6007E-08	-3.1358E-11	-4.4665E-08
2	0.0245812187	2.7873E-06	1.1339E-02	1.3699E-12	5.5730E-09	-5.4497E-12	-2.2170E-08
3	0.0070351926	1.3651E-05	1.9404E-01	-1.7622E-12	-2.5048E-08	1.8640E-11	2.6495E-07
4	0.0198719593	-9.9423E-06	-5.0032E-02	-1.4039E-11	-7.0647E-08	-4.0467E-10	-2.0364E-06
5	-0.0113855483	-7.8927E-06	6.9322E-02	9.3495E-12	-8.2117E-08	2.3594E-10	-2.0723E-06
6	-0.0285137171	-3.8429E-06	1.3477E-02	1.4446E-11	-5.0662E-08	5.0821E-10	-1.7823E-06
7	0.0005086987	1.3408E-06	2.6358E-01	-7.0467E-12	-1.3852E-06	-1.1293E-10	-2.2199E-05
8	0.1427562391	6.9009E-06	4.8340E-03	-3.6426E-11	-2.5516E-08	-1.2300E-09	-8.6163E-07
9	-0.0254696647	4.7337E-06	-1.8586E-02	6.9483E-12	-2.7281E-08	2.0961E-10	-8.2298E-07
10	-0.0467547417	-5.8803E-06	1.2577E-02	1.2354E-11	-2.6424E-08	4.5291E-10	-9.6870E-07
11	0.0182288605	-4.1825E-06	-2.2944E-02	-1.9162E-12	-1.0512E-08	-2.4871E-11	-1.3644E-07
12	0.0235721164	-1.4554E-06	-6.1742E-03	3.2766E-12	1.3900E-08	-6.3460E-12	-2.6922E-08
13	0.0302285093	-3.6853E-06	-1.2191E-02	1.1256E-11	3.7237E-08	4.2186E-12	1.3956E-08
14	0.0363683761	-1.6034E-05	-4.4088E-02	1.1913E-11	3.2757E-08	-3.0724E-12	-8.4480E-09
AoA	0.0008542099	-4.1651E-06	-4.8760E-01	-3.9028E-13	-4.5689E-08	-6.0492E-13	-7.0816E-08

All comparisons are performed on a single CPU. Thus, the FD gradient is computed in serial and incurs the highest wall-clock time to compute the gradient vectors, requiring upwards of 14 to 15 hours. When the FD gradient is computed in parallel for this case, it requires only 29 minutes and 32 seconds, which is approximately the same cost required to compute the flow solution. However, in this case an additional 30 CPUs are required for the FD gradient. Both the FD and SN gradients scale linearly with the number of design variables; however the SN method is typically more efficient than FD. Both the FD and SN methods have the advantage that they incur virtually no additional cost in order to compute the lift-constraint gradient. For the FD method, both the lift and drag are computed at each perturbed geometry state, and for the SN method, the linear systems given by (34) do not need to be solved again.

The two discrete adjoint approaches show significant improvement in efficiency and their cost is relatively independent of the number of design variables. The iterative (iAD) method requires approximately 16 minutes for the gradient computation, however, as explained in Section III.C.2, the cost of the iAD method approximately doubles when required to compute the lift-constraint. The non-iterative (nAD) method, on the other hand, incurs significantly less cost than all other methods. It requires approximately five minutes for the objective gradient and only one additional minute for the lift-constraint gradient, which is a result of reusing information that is stored during the objective function gradient evaluation. For these reasons, the nAD method is selected as the preferred gradient evaluation technique for free transitional flows. In the next chapter, we turn our attention to the design of NLF airfoils using the new gradient-based ASO framework.

Table 2. Time required to compute drag and lift gradients for a single optimization iteration with 15 design variables: RAE-2822, $Re = 15.7\times10^6$, $M = 0.6$, $AoA = 1^\circ$

	Wall-clock time (hh:mm:ss)			
Gradients	FD	SN	iAD	nAD
Drag Only	14:30:31	03:27:23	00:16:02	**00:04:56**
Drag + Lift	14:30:31	03:27:24	00:32:57	**00:05:57**

Table 3. Optimization cases

Case	Aircraft	Reynolds Number (Re)	Mach Number (M)	Lift Coefficient (C_l^*)
A	Cessna 172R	5.6×10^6	0.19	0.30
B	Dash-8 Q400	15.7×10^6	0.60	0.42
C	Boeing 737-8	20.3×10^6	0.71	0.50

V. Design Optimization Studies

V.A. Problem Definitions

To demonstrate the capabilities of the proposed optimization framework for the purpose of NLF airfoil design, single and multipoint optimizations are performed at conditions associated with subsonic and transonic commercial aircraft. In particular, we will be considering lift-constrained drag minimizations for which the optimization problem is defined as follows:

$$
\begin{aligned}
\min \quad & C_d\left(\mathbf{x}, \mathbf{Q}(\mathbf{x})\right) \\
\text{w.r.t.} \quad & \mathbf{x} \in \mathbb{R}^{N_\mathrm{D}} \\
\text{s.t.} \quad & C_l = C_l^* \\
& A_{\text{final}} \geq A_{\text{initial}} \\
& t_{0.03c} \geq 0.025c \\
& t_{0.98c} \geq 0.002c
\end{aligned}
$$

The objective is to minimize the total drag of the airfoil constrained by a user-specified lift target, C_l^*. As mentioned in Section I.B, we have selected a design objective and a set of constraints that aim to reflect the industry's aerodynamic design goals. We intentionally avoid the use of indirect objectives, such as those that focus specifically on delaying transition. In turn, the optimizer can better account for any design trade-offs that may exist (for example, between wave drag and friction drag). Additional inequality constraints are included for structural considerations; minimum thickness constraints near the leading and trailing edges are enforced, as well as an area constraint that ensures the final area of the airfoil is greater than or equal

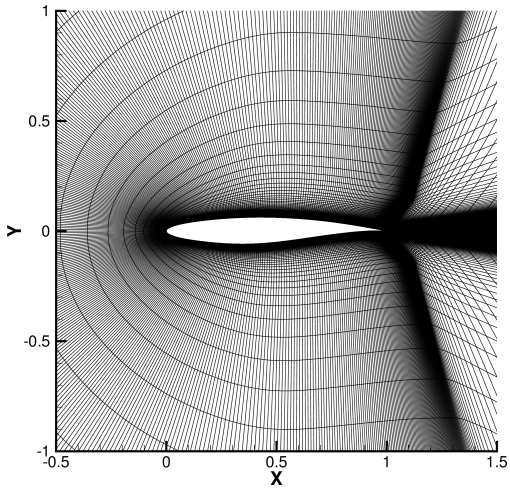

Figure 5. RAE-2822 C-grid with 575×224 nodes

to the initial area.

The initial geometry is taken as the RAE-2822 airfoil parametrized by seventeen B-spline control points, as previously shown in Figure 4. The control point located at the leading edge of the airfoil as well as the two coincident control points at the trailing edge are kept fixed throughout the optimization. The y-coordinates of the remaining 14 control points are used as the geometric design variables (marked by an "x"). The angle of attack is also included as an additional design variable. The computational grid consists of a 575×224 C-grid, shown in Figure 5, resulting from the grid convergence studies on the boundary-layer properties. All results were obtained using the scalar dissipation scheme, the compressible Bernoulli edge-finding method [25, 30], the smooth intermittency function given by (9) with a fixed transition length of 10% chord, and the non-iterative augmented adjoint gradient computation for free-transitional flows. Furthermore, it has been observed that the AHD criterion is generally less robust and less accurate than the e^N envelope criterion. Due to the importance of having robust, accurate, and deep convergence of the free-transition flow solver over a wide range of geometries, the e^N envelope criterion has been selected for the optimization results presented herein.

In the next section, we begin by considering single-point optimizations for the subsonic and transonic cases outlined in Table 3, which were selected to loosely approximate the cruise flight conditions of the Cessna 172R, the Bombardier Dash-8 Q400 turboprop, and the Boeing 737-800 turbofan.

The airfoils in this work have been investigated and optimized strictly under cruise flight conditions. More work is required to incorporate the low-speed, high-lift characteristics of the airfoils into the optimization framework. The multipoint optimization presented in Section IX considers the cruise segment of the Q400 flight envelope; however, the off-design performance at take-off, landing and dive conditions is not included. In practice, the protrusions created by high-lift devices, as well as engine pylons and flap-track fairings,

are typically detrimental to maintaining laminar flow. This motivates much of the ongoing research and development of slatless and morphing wing design [45], as well as highlighting an aerodynamic incentive to rear-mounted engines (further facilitating NLF on the lower surface) [46]. For practical NLF design, in addition to including a low-speed requirement, one should also consider multipoint optimization with varying critical N-factors (for reasons made clear in Section XI). Nonetheless, the various design studies presented in this work aim to quantify the potential benefits of optimization for NLF employing clean wings in cruise conditions. Ultimately the following studies serve as a proof-of-concept for the design procedure in general; they demonstrate that the methodology works and is capable of being used in a variety of contexts.

VI. Case A: Cessna 172R Skyhawk

The Cessna 172R Skyhawk is assumed to be cruising at 6000 ft, a speed of 120 knots, and a weight of 2200 lbs, corresponding to $Re = 5.6 \times 10^6$, $M = 0.19$, and $C_l^* = 0.3$. In this section we consider single-point optimization with results obtained using the e^N envelope transition criterion with $N_{\text{crit}} = 9$. In Table 4, a summary of the results comparing the initial and optimized airfoils is presented. Figure 6(a) compares the initial and optimized geometries and Figure 6(b) compares the pressure profiles. Note that in Figure 6(a), the geometries are rotated about the mid-chord position based on the angle of attack of the airfoil; the same is true for all such figures presented. The transition locations are indicated by the solid circles. The angle of attack decreased from an initial value of 0.75° to 0.19°, the lift constraint is satisfied, and the total drag is reduced by 35.1 drag counts, or 56%.

The ability of the optimizer to reduce drag by exploiting laminar-turbulent transition prediction is made evident by the aft movement of the transition points from 34% to 84% chord on the upper surface and 54% to 87% chord on the lower surface. The leading edge radius has decreased and the point of maximum thickness has been pushed significantly aft. As a result, the favourable pressure gradients are extended aft, in turn delaying transition.

VII. Case B: Bombardier Dash8-Q400

The design point for the Dash-8 Q400 is taken as point 6 from the multipoint optimization case (to be presented in Section IX). The Q400 is assumed to be cruising at a Mach number of 0.6, at an altitude of 23,000 ft, and a weight of 60755 lbs, corresponding to $Re = 15.7 \times 10^6$, $M = 0.6$, and $C_l^* = 0.42$. The results are obtained using the e^N envelope transition criterion with $N_{\text{crit}} = 9$. Table 5 provides a summary of the results comparing the initial and optimized airfoils. In this case, the angle of attack is decreased from an initial value of 1.14° to 0.66°, the lift constraint is again satisfied, and the total drag is reduced by 32.6 drag counts, or 54%. The transition point on the upper surface has been moved aft by over 50% chord, while the

Table 4. Case A summary of optimization results: $Re = 5.6\times10^6$, $M = 0.19$, $C_l^* = 0.3$

	C_d	C_{d_p}	C_{d_f}	C_l	C_m	$T_{\text{up}}(x/c)$	$T_{\text{lo}}(x/c)$	AoA
Initial	0.00556	0.00102	0.00454	0.3000	-0.06687	0.3349	0.5352	0.7498°
Optimized	0.00241	0.00061	0.00181	0.2999	-0.07514	0.8387	0.8669	0.1883°

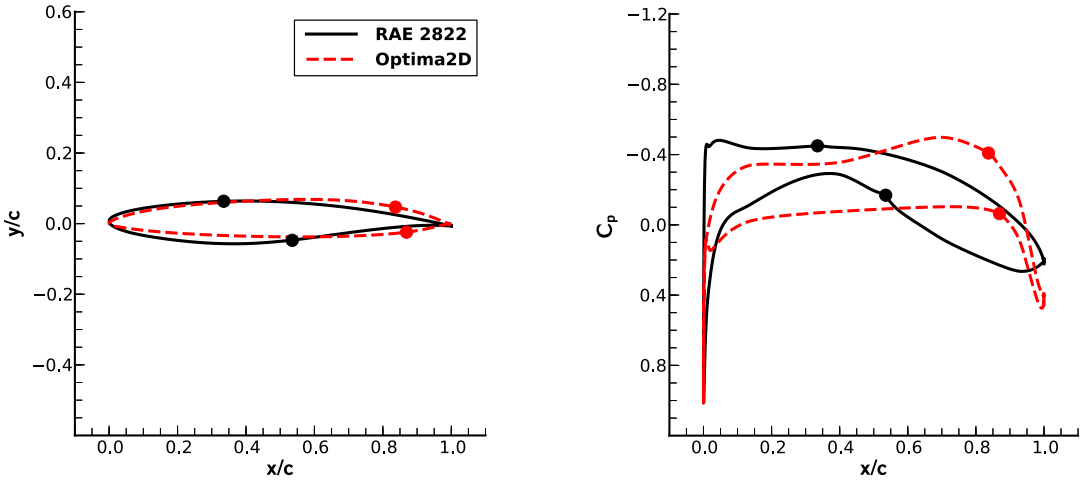

(a) Initial and optimized airfoils

(b) Initial and optimized pressure distributions

Figure 6. Case A optimization results: $Re = 5.6\times10^6$, $M = 0.19$, $C_l^* = 0.3$; **symbols indicate transition point locations**

lower surface transition point has moved aft approximately 20% chord.

Figure 7(a) compares the initial and optimized geometries; Figure 7(b) compares the pressure profiles. It can be observed that the optimizer was again successful in designing an airfoil with an extended favourable pressure gradient on both the upper and lower surfaces. Figure 7(c) provides the skin-friction distributions for this case, which serves to demonstrate the clear advantage of reduced skin-friction drag achieved by delaying the onset of transition. As in the previous case, the optimized geometry has a smaller leading edge radius and a point of maximum thickness that is further aft. The results demonstrate the ability of the optimizer to generate new NLF airfoils which would typically require considerable aerodynamic experience to design.

VIII. Case C: Boeing 737-800

The Boeing 737-800 has a wing sweep angle of 25°and is assumed to be cruising at 35000 ft, and a Mach number of 0.785, which corresponds to an effective Mach number of 0.71. The sectional lift coefficient is approximated as 0.5. Results are obtained using the e^N envelope transition criterion with $N_{\text{crit}} = 9$. Due to the transonic flight conditions, the optimization in this case is less robust. The flow solver may fail to converge if the transition locations are moved aft of a shockwave during the transition prediction procedure,

Table 5. Case B summary of optimization results: $Re = 15.7\times10^6$, $M = 0.6$, $C_l^* = 0.42$

	C_d	C_{d_p}	C_{d_f}	C_l	C_m	$T_{\text{up}}(x/c)$	$T_{\text{lo}}(x/c)$	AoA
Initial	0.00598	0.00194	0.00405	0.4200	-0.08129	0.1480	0.4912	1.1424°
Optimized	0.00272	0.00095	0.00178	0.4199	-0.08247	0.7232	0.7685	0.6613°

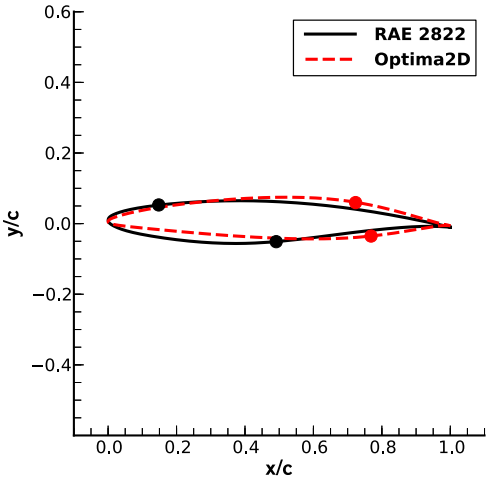

(a) Initial and optimized airfoils

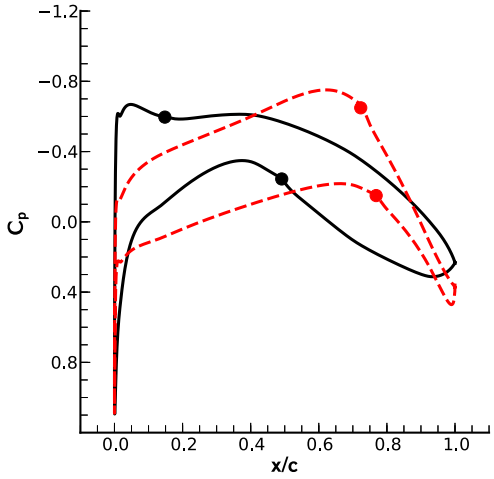

(b) Initial and optimized pressure distributions

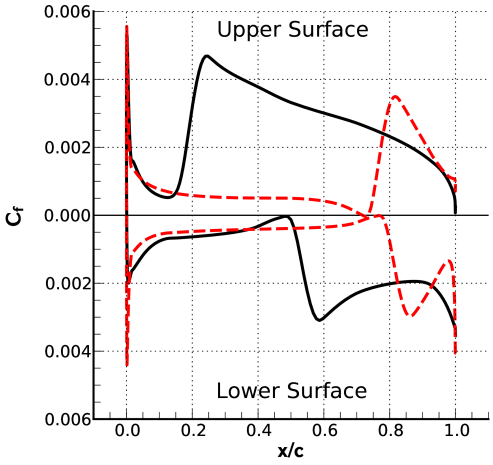

(c) Initial and optimized skin-friction distributions

Figure 7. Case B optimization results; $Re = 15.7\times10^6$, $M = 0.6$, $C_l^* = 0.42$**; symbols indicate transition point locations**

in turn causing unsteady flow separation. Modifications to the transition prediction algorithm for increased robustness have been discussed in Section II.D.1.

Table 6 provides a summary of the results comparing the initial and optimized airfoils. The angle of attack in this case is decreased from an initial value of 1.13° to −0.25°, the lift constraint is satisfied, and the total drag is reduced by 25.8 drag counts, or 42%. The transition point on the upper surface was moved aft from 21% to 74% chord, and from 47% to 50% chord on the lower surface. Figure 8(a) compares the initial and optimized geometries; Figure 8(b) compares the pressure profiles. In this case, the optimizer

Table 6. Case C summary of optimization results: $Re = 20.3\times10^6$, $M = 0.71$, $C_l^* = 0.5$

	C_d	C_{d_p}	C_{d_f}	C_l	C_m	$T_{\text{up}}(x/c)$	$T_{\text{lo}}(x/c)$	AoA
Initial	0.00617	0.00259	0.00358	0.4995	-0.09427	0.2090	0.4740	1.1266°
Optimized	0.00359	0.00146	0.00214	0.5014	-0.16261	0.7441	0.5006	-0.2487°

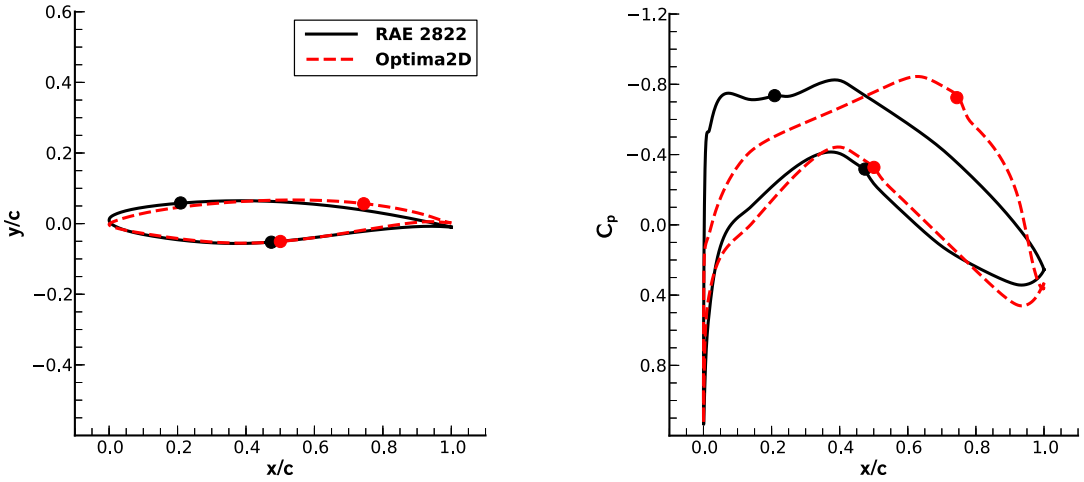

(a) Initial and optimized airfoils

(b) Initial and optimized pressure distributions

Figure 8. Case C optimization results; $Re = 20.3\times10^6$, $M = 0.71$, $C_l^* = 0.5$**; symbols indicate transition point locations**

is successful in designing a shock-free transonic NLF airfoil, in turn, significantly reducing the total drag. While the optimizer is able to delay transition significantly on the upper surface, the lower surface transition location remains near the mid-chord position. With the favourable pressure gradient on the top surface extended further aft than that of the lower surface, the airfoil is more heavily aft-loaded. The aft-loading, in turn, results in a higher negative pitching moment and future work will consider the addition of a pitching moment constraint for transonic NLF applications.

IX. Multipoint Optimization

Here we consider a multipoint optimization at a range of cruise conditions associated with the Dash-8 Q400 aircraft. A nine-point stencil, presented in Table 7, is defined by varying the aircraft weight and Mach number. This is done to reduce the sensitivity of the final optimized shape to any perturbations in the flight conditions encountered during cruise and to enable efficient operation within this envelope. The aircraft is assumed to have a take-off weight equal to the Q400's maximum take-off weight of 64500 lbs. Given a typical payload, the usable fuel on board (at take-off) is approximated to be 7500 lbs. The three aircraft weights considered in the multipoint stencil are calculated from a 10%, 50% and 90% fuel burn, which loosely approximate the beginning, middle, and end of cruise. The three Mach numbers considered are 0.6, 0.54, and

Table 7. Design points and weighting for multipoint optimization

Design Pt.	Quadrature Weight ($\mathcal{T}$)	Aircraft Weight (W) [lbs]	Mach No. (M)	Reynolds No. (Re)	Lift Coefficient (C_l^*)
1	1	63757	0.48	12.5×10^6	0.68
2	2	63757	0.54	14.1×10^6	0.54
3	1	63757	0.60	15.7×10^6	0.44
4	2	60754	0.48	12.5×10^6	0.65
5	4	60754	0.54	14.1×10^6	0.51
6	2	60754	0.60	15.7×10^6	0.42
7	1	57751	0.48	12.5×10^6	0.62
8	2	57751	0.54	14.1×10^6	0.49
9	1	57751	0.60	15.7×10^6	0.40

0.48, which roughly correspond to the high-speed, intermediate, and long-range design speeds of the Q400, respectively. Given the range of weights and Mach numbers, and assuming a constant cruising altitude of 23000 ft, we can then compute the corresponding range of Reynolds numbers and lift constraints presented in Table 7. The results are obtained using the e^N envelope transition criterion with $N_{\text{crit}} = 9$.

Recall from Section III.D that the design objective given by (31) is an approximation to the weighted integral given by (30). Although any design priority weighting may be selected as desired, here we make the assumption that all design points are of equal importance, that is, $\mathcal{Z}(W_i, M_j) = 1$ for all i and j. Table 7 also presents the quadrature weights $\mathcal{T}$ used to approximate (30) using the trapezoidal quadrature rule.

Table 8 provides a summary of the results comparing the initial and optimized airfoils, along with the various angles of attack. The lift constraint has been satisfied and the drag reduced at each operating point. The flight conditions and lift constraint of design point 6 correspond to the Q400 single-point optimization presented in Section VII. Figure 9(a) compares the single-point and multipoint optimized geometries for design point 6, and Fig 9(b) compares the pressure distributions. Comparing the optimized designs, it is clear that the single and multipoint results differ. The multipoint optimization has transition points that are approximately 5% further upstream when compared to the single-point optimization of Case B. Furthermore, while the total drag was reduced by 55% in the single-point optimization, it was reduced by 50% in the multipoint optimization. This illustrates that the added robustness in the design (now optimized over a range of conditions) is indeed a compromise. It also exemplifies the importance of the designer's role in carefully selecting and weighting the design points appropriately. For example, if the Q400 normally cruises at the high-speed Mach number of 0.60, then the designer might choose to place more importance on those operating points. Finally, we again emphasize that a full aerodynamic design requires more work to incorporate the high-lift requirements, dive conditions, and other factors effecting the overall aerodynamic performance of the design. The present study simply demonstrates the effectiveness of the methodology in

Table 8. Summary of multipoint optimization results

Design Pt.		C_d	C_{d_p}	C_{d_f}	C_l	C_m	$T_{\text{up}}(x/c)$	$T_{\text{lo}}(x/c)$	AoA
1	Initial	0.00803	0.00345	0.00458	0.6795	-0.07315	0.0172	0.5393	3.5050°
	Optimized	0.00453	0.00211	0.00241	0.6799	-0.08278	0.5509	0.7767	2.5651°
2	Initial	0.00692	0.00253	0.00439	0.5400	-0.07691	0.0620	0.5134	2.2177°
	Optimized	0.00328	0.00128	0.00200	0.5399	-0.08434	0.6656	0.7583	1.2498°
3	Initial	0.00613	0.00205	0.00408	0.4400	-0.08123	0.1328	0.4932	1.2852°
	Optimized	0.00304	0.00105	0.00199	0.4400	-0.08730	0.6664	0.7297	0.3184°
4	Initial	0.00779	0.00323	0.00456	0.6494	-0.07328	0.0199	0.5356	3.2717°
	Optimized	0.00393	0.00174	0.00219	0.6502	-0.08252	0.6194	0.7741	2.3059°
5	Initial	0.00670	0.00234	0.00436	0.5100	-0.07704	0.0763	0.5103	1.9920°
	Optimized	0.00318	0.00117	0.00200	0.5100	-0.08347	0.6685	0.7558	1.0383°
6	Initial	0.00598	0.00194	0.00405	0.4201	-0.08129	0.1479	0.4912	1.1430°
	Optimized	0.00300	0.00100	0.00200	0.4202	-0.08662	0.6683	0.7226	0.1875°
7	Initial	0.00761	0.00298	0.00463	0.6200	-0.07355	0.0232	0.5321	3.0357°
	Optimized	0.00368	0.00155	0.00213	0.6201	-0.08191	0.6421	0.7717	2.0713°
8	Initial	0.00656	0.00222	0.00434	0.4900	-0.07710	0.0860	0.5082	1.8419°
	Optimized	0.00311	0.00111	0.00200	0.4899	-0.08287	0.6705	0.7543	0.8963°
9	Initial	0.00584	0.00183	0.00401	0.4000	-0.08133	0.1634	0.4889	1.0000°
	Optimized	0.00301	0.00095	0.00206	0.4001	-0.08590	0.6701	0.6977	0.0527°

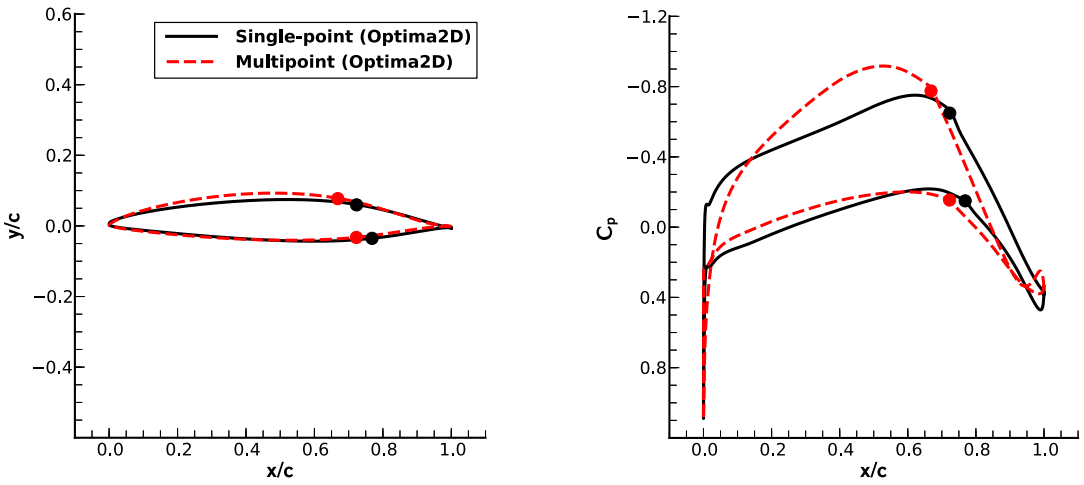

(a) Initial and optimized airfoils

(b) Point 6: Initial and optimized pressure distributions

Figure 9. Comparison of single-point and multipoint optimization results (design point 6)

a multipoint approach to design.

X. Pareto Front Design Study

A Pareto front can provide useful insight into the trade-offs involved in the design of NLF airfoils. While the multipoint optimization case (presented in Section IX) is useful for designing an airfoil that performs

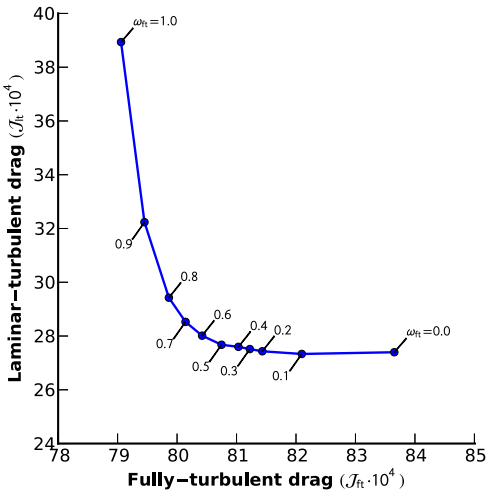

Figure 10. Pareto front study, Case B: $Re = 15.7\times10^6$, $M = 0.6$, $C_l^* = 0.42$

well over a range of cruise flight conditions, here we consider the aerodynamic performance of NLF airfoils when or if transition occurs inadvertently at the leading edge of the airfoil.

Following the work of Driver and Zingg [17], a Pareto front may be formed by minimizing a weighted sum objective, $\mathcal{J}$, defined as

$$\mathcal{J} = \omega_{\text{ft}}\mathcal{J}_{\text{ft}} + (1-\omega_{\text{ft}})\mathcal{J}_{\text{lt}}\,, \tag{35}$$

where $\mathcal{J}_{\text{ft}}$ and $\mathcal{J}_{\text{lt}}$ represent the drag coefficients under fully-turbulent and laminar-turbulent (i.e. free transition) conditions, respectively. Each point on the Pareto front represents a two-point design problem in which we minimize $\mathcal{J}$ for a given weighting factor, ω_{ft}, where $0 \le \omega_{\text{ft}} \le 1$. The calculation of the two operating conditions ($\mathcal{J}_{\text{ft}}$ and $\mathcal{J}_{\text{lt}}$) in turn requires two flow solutions, each at their respective angle of attack. Furthermore, both operating conditions are constrained to meet the same lift target (set to $C_l^* = 0.42$ for Case B) to ensure sufficient lift generation at both conditions for every optimal point.

The computed Pareto front is shown in Figure 10 and clearly captures the advantages of favouring one operating condition over the other. As expected, the drag count values under laminar-turbulent conditions are significantly less than the fully-turbulent operating conditions. The Pareto front demonstrates that when an airfoil designed strictly for laminar-turbulent conditions (that is, $\omega_{\text{ft}} = 0$) is operating under fully-turbulent conditions, it has a drag count of approximately 84, as compared to 79 counts for an airfoil designed and operated under fully-turbulent conditions ($\omega_{\text{ft}} = 1$); a relative drag penalty of approximately 6%. On the other hand, when an airfoil designed strictly for fully-turbulent conditions is operating under laminar-turbulent conditions it has a drag count of approximately 39, as compared to 27 counts for an airfoil designed and operated under laminar-turbulent conditions; a relative drag penalty of approximately 44%. The remaining points on the Pareto front allow the designer to select an appropriate optimal geometry depending on their

needs and conservatism. Airfoils optimized using ω_{ft} values in the range of $0.2 \leq \omega_{\text{ft}} \leq 0.7$ represent a good compromise in performance between the two operating conditions.

XI. Robustness to Uncertainty in Location of Transition

The design of NLF airfoils should be robust to the uncertainties in the locations of the transitions points. The sources of these uncertainties can be divided into two categories: (i) uncertainty in the disturbance environment, and (ii) uncertainty in the prediction of the transition locations. Uncertainty in the disturbance environment can stem from discrepancies between wind-tunnel and in-flight freestream turbulence intensities (T_u), as well as many other factors that can affect the transition process, such as acoustic disturbances, vibrations, and surface roughness [47].

When considering the robust design of NLF airfoils, both sources of uncertainty are important, and both can be reflected in the selection of the critical N-factor. It is not clear that an airfoil optimized under one set of conditions, reflected in the critical N-factor, will perform well under other conditions, i.e. with a different critical N-factor. This is addressed in this section by first examining the sensitivity to the critical N-factor and then proposing a technique to enable the design of airfoils with robust performance over a range of critical N-factors.

XI.A. Sensitivity to the Critical N-factor

To examine the sensitivity to the critical N-factor, we repeat the single-point optimization performed in Section VII by specifying different values for N_{crit}. Recall that the previously presented single-point optimization of the Q400 (Section VII) assumed a critical N-factor of 9. In the first case, we decrease the critical N-factor to a value of 7, which implies that transition will occur further upstream for the same geometry and flight conditions. In the second scenario, we increase the critical N-factor to a value of 11, which implies the opposite trend.

The results of the optimizations are presented in Table 9. The labelling is such that SP7 represents the optimized geometry from the single-point optimization performed at $N_{\text{crit}} = 7$. The performance of the single-point optimizations at different N_{crit} values (for example, SP7 at $N_{\text{crit}} = 9$) will be discussed in the coming sections, as will the multipoint results. For the single-point optimizations, it can be seen that the lift target is met and the optimal drag coefficients decrease with increasing N_{crit}; the difference in drag between $N_{\text{crit}} = 7$ and $N_{\text{crit}} = 11$ is approximately 1.2 counts. It can also be observed that the optimal geometries have transition points on the upper surface that are further aft as we increase N_{crit} (as expected). For the $N_{\text{crit}} = 11$ case, the optimizer takes a slightly lower angle of attack, resulting in an optimal geometry with an upper surface transition point that is 5-7% chord further downstream and a lower surface transition point

Table 9. Summary of single-point optimizations, off-design performance, and multipoint optimization over a range of critical N-factor values

Geometry	N_{crit}	C_d	C_{d_p}	C_{d_f}	C_l	C_m	$T_{\text{up}}(x/c)$	$T_{\text{lo}}(x/c)$	AoA
Initial	7	0.00612	0.00198	0.00414	0.4200	-0.08101	0.1206	0.4816	1.1531°
SP7	7	0.00276	0.00092	0.00184	0.4200	-0.08480	0.7124	0.7439	0.5953°
SP7	9	— did not converge due to flow separation —							
SP7	11	— did not converge due to flow separation —							
Initial	9	0.00598	0.00194	0.00405	0.4200	-0.08129	0.1480	0.4912	1.1424°
SP9	9	0.00272	0.00095	0.00178	0.4199	-0.08247	0.7232	0.7685	0.6613°
SP9	7	0.00281	0.00095	0.00186	0.4185	-0.08216	0.7111	0.7546	0.6613°
SP9	11	— did not converge due to flow separation —							
Initial	11	0.00583	0.00189	0.00394	0.4200	-0.08159	0.1783	0.4985	1.1300°
SP11	11	0.00264	0.00095	0.00168	0.4200	-0.12140	0.7780	0.7405	-0.0422°
SP11	7	0.00388	0.00122	0.00265	0.4062	-0.11163	0.7441	0.3956	-0.0422°
SP11	9	0.00272	0.00095	0.00178	0.4174	-0.12077	0.7661	0.7275	-0.0422°
MP	7	0.00297	0.00091	0.00207	0.4203	-0.08559	0.6762	0.7045	0.5707°
MP	9	0.00286	0.00089	0.00197	0.4204	-0.08581	0.6927	0.7194	0.5631°
MP	11	0.00281	0.00090	0.00191	0.4203	-0.08591	0.7010	0.7280	0.5594°

*SP7 = geometry from single-point optimization at $N_{\text{crit}}=7$
*SP9 = geometry from single-point optimization at $N_{\text{crit}}=9$
*SP11 = geometry from single-point optimization at $N_{\text{crit}}=11$
*MP = geometry from multipoint optimization (Section XI.B)

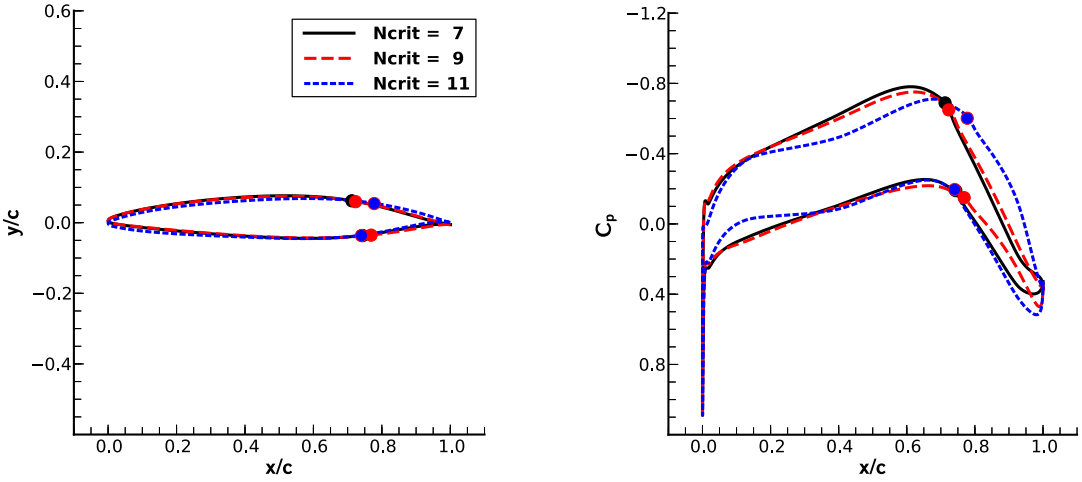

(a) Optimized airfoil geometries

(b) Optimized pressure distributions

Figure 11. Comparison of single-point optimizations performed at different critical N-factors values

that is approximately 1-3% further upstream, as compared to the other two cases.

A comparison of the optimized geometries and pressure profiles is presented in Figure 11. In an attempt to maintain laminar flow, the optimizer produces steeper favourable pressure gradients as the critical N-factor decreases. Qualitatively, the optimized geometries and angles of attack are very similar; however, the variation in N_{crit} produces important changes to the geometry that alter the point at which pressure recovery begins and transition occurs.

XI.A.1. Performance of Single-point Optimizations at Different Critical N-factors

Table 9 also presents the results of a post-optimality study on the performance of the three single-point cases at different critical N-factors. Flow solutions are computed for each combination of N_{crit} with each optimized airfoil and angle of attack. Typically, one would expect that optimizing using a lower critical N-factor is assumed to be more conservative and robust to factors that may prematurely trip the flow. However, optimizations performed at too low a value of N_{crit} can result in an airfoil that is not robust to the opposite scenario; that is, one in which a higher N_{crit} is encountered. For example, if we take the SP7 airfoil and angle of attack (optimized with $N_{\text{crit}} = 7$) and attempt a flow solution at $N_{\text{crit}} = 9$ or 11, the laminar boundary layer does not transition soon enough to avoid flow separation. The same behaviour is observed when we take the SN9 airfoil and attempt a flow solution at $N_{\text{crit}} = 11$. As indicated in Table 9, for these cases our steady flow solver is not able to converge due to the unsteadiness of the separated flow. Needless to say, this type of flow separation should be avoided in NLF design due to the significantly increased pressure drag that results.

If, on the other hand, we take the airfoils designed at the higher values of N_{crit} and perform flow analyses at lower values of N_{crit}, then flow separation is not an issue. Depending on the optimized pressure profiles, the performance degradation when operating at a lower than expected N_{crit} may or may not be significant. For example, when the SP9 airfoil is analyzed at $N_{\text{crit}} = 7$, the transition points move slightly further upstream, but the airfoil continues to perform well. The same is true for the SP11 airfoil when analyzed at $N_{\text{crit}} = 9$. However, when the SP11 airfoil is analyzed at $N_{\text{crit}} = 7$, a noticeable drag increase of 12.4 counts results due to the lower surface transition point being much further upstream: 39.6% chord for $N_{\text{crit}} = 7$ as compared to 74.4% chord for $N_{\text{crit}} = 11$. The reason for this can be observed in the lower surface pressure profile, which contains a dip just upstream of the mid-chord region. This dip presents a short region of mild adverse pressure gradient that is sufficient to trigger transition at the lower critical N-factor but not at the higher values. In general, these results imply that the single-point optimizations (while qualitatively similar) are not particularly robust to the uncertainty in the specification of N_{crit}. In the next section we propose an NLF design strategy that aims to reduce this sensitivity.

XI.B. Robust Design Over a Range of Critical N-factors

To address the concerns raised in the previous section, we propose the use of multipoint optimization over a range of critical N-factors. The objective is to reduce the sensitivity of the final NLF airfoil to the uncertainty in the transition locations (*viz.* the specified N_{crit} values). The same weighted integral approach presented

in Section III.D is employed, with the objective defined as

$$\mathcal{J} = \int_{N_1}^{N_2} C_d\,(N)\,\mathcal{Z}\,(N)\,dN = \sum_{i=1}^{p} \mathcal{T}_i\,C_d\,(N_i)\,\mathcal{Z}\,(N_i)\,\Delta N\,, \tag{36}$$

where N is used to denote N_{crit} (for clarity), and p is the number of operating points, each with a different N.

As a demonstration, we shall consider a combination of the three single-point cases ($p=3$) presented in the previous section. The objective is evaluated using the Q400 flight conditions with $N=\{7,9,11\}$, and the corresponding trapezoidal quadrature weighting of $\mathcal{T}=\{\frac{1}{2},1,\frac{1}{2}\}$. All points are assumed to be equally important and given a design-point weighting of $\mathcal{Z}(N_i)=1$. Note that the designer is free to adjust the design-point weighting function as desired.

At the bottom of Table 9, a summary of the multipoint optimization is presented (labelled MP). It can be observed that the optimizer is able to design an airfoil that minimizes the weighted drag objective over all three N_{crit} conditions, while meeting the lift-constraint and keeping the flow attached. The penalty in designing a multipoint airfoil over the single-point airfoils is also quantified for each value of N_{crit}; the $N_{\text{crit}}=7$ case incurs the largest drag penalty of 2.1 counts. However, recall from the previous section that when the SP7 and SP9 geometries were run at the higher N_{crit} values, the laminar boundary layer was observed to separate (and the flow solver failed to converge).

Figure 12(a) compares the optimal geometry from the multipoint optimization to the optimal geometry of the $N_{\text{crit}}=9$ single-point case. Figures 12(b)–12(d) compare the single-point and multipoint pressure profiles for each value of N_{crit}. The geometry and pressure profiles that result from the multipoint optimization are such that the transition locations do not vary significantly with a change in N_{crit}. For the multipoint case, the optimizer produces a geometry and angle of attack for which (i) the point of pressure recovery occurs further upstream, (ii) the initial pressure recovery occurs more gradually (particularly on the lower surface), in turn reducing the steepness of the adverse pressure gradient, and (iii) there are no dips present in the pressure profiles (as observed in the $N_{\text{crit}}=11$ case), which could prematurely transition the flow. These differences, while subtle, help to design an NLF airfoil that avoids flow separation and performs well at all three values of N_{crit}. Indeed, the more gradual pressure recovery is strikingly similar to the so-called *transition ramps* used by experienced designers as a means of controlling how and where transition occurs [48–50]. These results are very promising and demonstrate the feasibility and importance of the multipoint N-factor approach in designing NLF airfoils that are robust to the uncertainty in the transition locations.

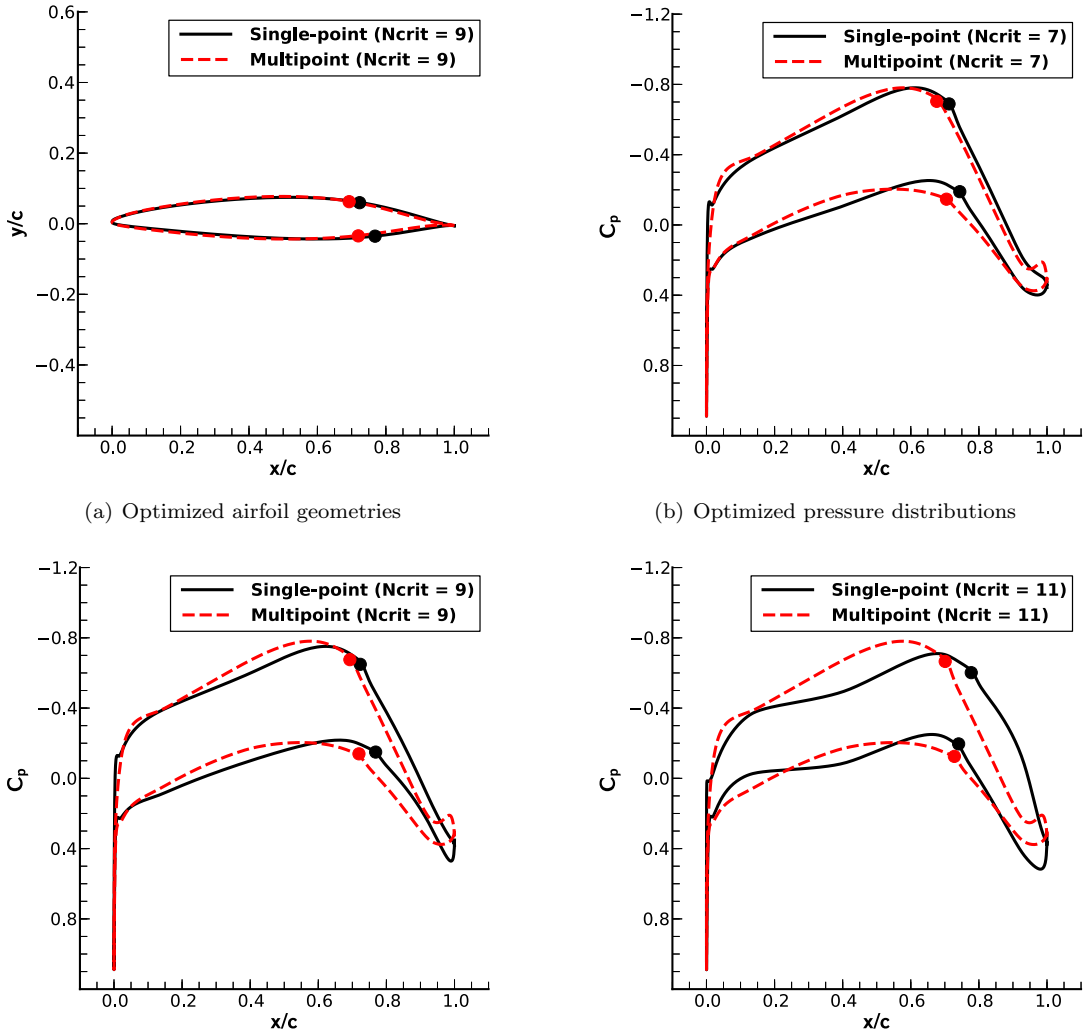

(a) Optimized airfoil geometries

(b) Optimized pressure distributions

(c) Optimized pressure distributions

(d) Optimized pressure distributions

Figure 12. Comparison of single-point and multipoint optimizations with different critical N-factor values

XII. Conclusions

A two-dimensional RANS solver making use of the Spalart-Allmaras turbulence model has been extended to incorporate an iterative laminar-turbulent transition prediction methodology. With reasonable grid density, the boundary-layer properties can be computed directly from the Navier-Stokes solution with sufficient accuracy. The compressible form of the AHD criterion and the simplified e^N envelope method have been implemented, verified, and validated by comparison to numerical and experimental data.

The RANS solver was subsequently employed in a gradient-based sequential quadratic programming shape optimization framework using the SNOPT optimization suite. The gradients are evaluated using a new augmented discrete-adjoint formulation for transition prediction in a RANS solver. Two solution strategies have been developed and verified for the augmented system, and their accuracies and efficiencies have been verified and compared. The resulting optimization framework has been applied to the design

of natural-laminar-flow airfoils using single and multipoint optimizations, as well as a Pareto front study. Finally, a multipoint N-factor approach has been proposed and demonstrated to increase the robustness of NLF design to the uncertainty in the transition locations. Such applications demonstrate the practicality of using high-fidelity aerodynamic shape optimization as an effective NLF design tool. Future work will consider the extension of the current methodology to three dimensions, incorporating a crossflow transition criterion.

XIII. Acknowledgements

The authors gratefully acknowledge the financial assistance of the Ontario Government, Mathematics of Information Technology and Complex Systems, Canada Research Chairs Program, Bombardier Aerospace, and the University of Toronto.

References

[1]Marburger, J. H., "National Aeronautics Research and Development Plan," Technical report, National Science and Technology Council, February 2010.

[2]Fujino, M., Yoshizaki, Y., and Kawamura, Y., "Natural-Laminar-Flow Airfoil Development for a Lightweight Business Jet," *Journal of Aircraft*, Vol. 40, No. 4, July 2003, pp. 609–615.

[3]Campbell, R., Campbell, M., and Streit, T., "Progress Toward Efficient Laminar Flow Analysis and Design," *29th AIAA Applied Aerodynamics Conference*, No. AIAA–2011–3527, Honolulu, Hawaii, Jun 2011.

[4]Zingg, D. W. and Godin, P., "A perspective on turbulence models for aerodynamic flows," *International Journal of Computational Fluid Dynamics*, Vol. 23, No. 4, April 2009, pp. 327–335.

[5]Reed, H. L. and Saric, W. S., "Transition Mechanisms for Transport Aircraft," *38th Fluid Dynamics Conference and Exhibit*, No. AIAA–2008–3743, Seattle, Washington, June 2008.

[6]Arnal, D., Casalis, G., and Houdeville, R., "Practical Transition Prediciton Methods: Subsonic and Transonic Flows," *VKI Lecture Series: Advances in Laminar-Turbulent Transition Modeling*, January 2009.

[7]Cliquet, J., Houdeville, R., and Arnal, D., "Application of Laminar-Turbulent Transition Criteria in Navier-Stokes Computations," *AIAA Journal*, Vol. 46, No. 5, May 2008, pp. 1182–1190.

[8]Cebeci, T. and Cousteix, J., *Modeling and Computation of Boundary-Layer Flows*, Springer, Long Beach, 2nd ed., 2005.

[9]Langtry, R. B. and Menter, F. R., "Transition Modeling for General CFD Applications in Aeronautics," *43rd AIAA Aerospace Sciences Meeting and Exhibit*, No. AIAA–2005–522, Reno, Nevada, 10–13 January 2005.

[10]Langtry, R. B. and Menter, F. R., "Correlation-Based Transition Modeling for Unstructured Parallelized Computational Fluid Dynamics Codes," *AIAA Journal*, Vol. 47, No. 12, December 2009, pp. 2894–2906.

[11]Medida, S. and Baeder, J. D., "Application of the Correlation based γ–Re_{θ_t} Transition Model to the Spalart-Allmaras Turbulence Model," *20th AIAA Computational Fluid Dynamics Conference*, No. AIAA–2011–3979, Honolulu, Hawaii, June 2011.

[12]Aranake, A., Lakshminarayan, V., and Duraisamy, K., "Assessment of Transition Model and CFD Methodology for Wind

Turbine Flows," *42nd AIAA Fluid Dynamics Conference and Exhibit*, No. AIAA–2012–2720, New Orleans, Louisiana, June 2012.

[13]Krimmelbein, N. and Radespiel, R., "Transition prediction for three-dimensional flows using parallel computation," *Computers & Fluids*, Vol. 38, No. 1, 2009, pp. 121–136.

[14]Streit, T., Horstmann, H., Shraut, G., Hein, S., Fey, U., Egmai, Y., Perraud, J., Salah El Din, I., Cella, U., and Quest, J., "Complementary Numerical and Experimental Data Analysis of the ETW Telfona Pathfinder Wing Transition Tests," *49th Aerospace Sciences Meeting and Exhibit*, No. AIAA–2011–881, Orlando, Florida, January 2011.

[15]Langtry, R., "Extending the $\gamma - Re_\theta$ Correlation based Transition Model for Crossflow Effects (Invited)," *45th AIAA Fluid Dynamics Conference*, No. AIAA–2015–2474, Dallas, TX, June 2015.

[16]Krumbein, A., Krimmelbein, N., Grabe, C., and Shengyang, N., "Development and Application of Transition Prediction Techniques in an Unstructured CFD Code (Invited)," *45th AIAA Fluid Dynamics Conference*, No. AIAA–2015–2476, Dallas, TX, June 2015.

[17]Driver, J. and Zingg, D. W., "Numerical Aerodynamic Optimization Incorporating Laminar-Turbulent Transition Prediction," *AIAA Journal*, Vol. 45, No. 8, August 2007, pp. 1810–1818.

[18]Lee, J. and Jameson, A., "Natural-Laminar-Flow Airfoil and Wing Design by Adjoint Method and Automatic Transition Prediction," *47th AIAA Aerospace Sciences Meeting and Exhibit*, No. AIAA–2009–897, Orlando, Florida, 5–8 January 2009.

[19]Khayatzadeh, P. and Nadarajah, S. K., "Aerodynamic Shape Optimization of Natural Laminar Flow (NLF) Airfoils," *50th AIAA Aerospace Sciences Meeting*, No. AIAA–2012–0061, Nashville, Tennessee, 9–12 January 2012.

[20]Zahle, F., Bak, C., Srensen, N. N., Vronsky, T., and Gaudern, N., "Design of the LRP airfoil series using 2D CFD," *Journal of Physics: Conference Series*, Vol. 524, No. 012020, Jun 2014.

[21]Jing, L., Zhenghong, G., Jiagntao, H., and Ke, Z., "Robust design of NLF airfoils," *Chinese Journal of Aeronautics*, Vol. 26, No. 2, April 2013, pp. 309–318.

[22]Zhao, K., Gao, Z., and Huang, J., "Robust design of natural laminar flow supercritical airfoil by multi-objective evolution method," *Appl. Math. Mech.-Engl. Ed.*, Vol. 35, No. 2, Jan 2014, pp. 191202.

[23]Robitaille, M., Mosahebi, A., and Laurendeau, E., "Design of adaptive transonic laminar airfoils using the $\gamma - Re_{\theta_t}$ transition model," *Aerospace Science and Technology*, Vol. 46, Oct 2015, pp. 60–71.

[24]Wang, X., Cai, J., Liu, C., and Hu, Z., "Airfoil Optimization Based on Rapid Transition Prediction," *56th AIAA/ASCE/AHS/ASC Structures, Structural Dynamics, and Materials Conference*, No. AIAA–2015–0400, Jan 2015.

[25]Rashad, R. and Zingg, D. W., "Toward High-Fidelity Aerodynamic Shape Optimization for Natural Laminar Flow," *21st AIAA Computational Fluid Dynamics Conference*, No. AIAA–2013–2583, San Diego, CA, June 2013.

[26]Nemec, M. and Zingg, D. W., "Newton-Krylov Algorithm for Aerodynamic Design Using the Navier-Stokes Equations," *AIAA Journal*, Vol. 40, No. 6, June 2002, pp. 1146–1154.

[27]Jameson, A., Schmidt, W., and Turkel, E., "Numerical solution of the Euler equations by finite volume methods using Runge-Kutta time-stepping schemes," *14th AIAA Fluid and Plasma Dynamics Conference*, No. AIAA–81–1259, Palo Alto, California, June 1981.

[28]Swanson, R. and Turkel, E., "On central-difference and upwind schemes," *Journal of Computational Physics*, Vol. 101, No. 2, Aug 1992, pp. 292–306.

[29]Spalart, P. and Allmaras, S., "A One-Equation Turbulence Model for Aerodynamic Flows," *30th AIAA Aerospace Sciences Meeting & Exhibit*, No. AIAA–092–0439, Reno, NV, January 1992.

[30]Nebel, C., Radespiel, R., and Wolf, T., "Transition Prediction for 3D Flows Using a Reynolds-averaged Navier-Stokes Code and N-Factor Methods," *33rd AIAA Fluid Dynamics Conference and Exhibit*, No. AIAA–2003–3593, Jun 2003.

[31]Drela, M. and Giles, M. B., "Viscous-inviscid analysis of transonic and low Reynolds number airfoils," *AIAA Journal*, Vol. 25, No. 10, Oct 1987, pp. 1347–1355.

[32]Arnal, D., Houdeville, R., Seraudie, A., and Vermeersh, O., "Overview of laminar- turbulent transition investigations at ONERA Toulouse," *41st AIAA Fluid Dynamics Conference and Exhibit*, No. AIAA–2011–3074, Honolulu, Hawaii, June 2011.

[33]Brodeur, R. R. and van Dam, C. P., "Transition Prediction for a Two-Dimensional Reynolds-averaged Navier-Stokes Method Applied to Wind Turbine Airfoils," *Wind Energy*, Vol. 4, No. 2, October 2001, pp. 61–75.

[34]Krumbein, A., "On Modeling of Transitional Flow and its Application on a High Lift Multi-Element Airfoil Configuration," *41st Aerospace Sciences Meeting and Exhibit*, No. AIAA–2003–724, Reno, Nevada, January 2003.

[35]Mayda, E., *Boundary Layer Transition Prediction for Reynolds-Averaged Navier-Stokes Methods*, Ph.D. thesis, University of California, Davis, 2007.

[36]Krumbein, A., Krimmelbein, N., and Schrauf, G., "Automatic Transition Prediction in Hybrid Flow Solver, Part 1: Methodology and Sensitivities," *Journal of Aircraft*, Vol. 46, No. 4, July 2009, pp. 1176–1190.

[37]Dhawan, S. and Narasimha, R., "Some Properties of Boundary-Layer Flow During the Transition from Laminar to Turbulent Motion," *Journal of Fluid Mechanics*, Vol. 3, 1958, pp. 418–436.

[38]Gill, P. E., Murray, W., and Saunders, M. A., "SNOPT: An SQP Algorithm for Large-Scale Constrained Optimization," *SIAM Review*, Vol. 47, No. 1, Jan 2005, pp. 99–131.

[39]Jameson, A., Pierce, N. A., and Martinelli, L., "Optimum Aerodynamic Design Using the Navier-Stokes Equations," *Theoretical and Computational Fluid Dynamics*, Vol. 10, No. 1, 1998, pp. 213–237.

[40]Krumbein, A., "e^N transition prediction for 3D wing configurations using database methods and a local, linear stability code," *Aerospace Science and Technology*, Vol. 12, No. 8, December 2008, pp. 592–598.

[41]Squire, W. and Trapp, G., "Using Complex Variables to Estimate Derivatives of Real Functions," *SIAM Review*, Vol. 40, No. 1, January 1998, pp. 110–112.

[42]Rashad, R. and Zingg, D. W., "Aerodynamic Shape Optimization for Natural Laminar Flow Using a Discrete-Adjoint Approach," *22nd AIAA Computational Fluid Dynamics Conference*, No. AIAA–2015–3061, Dallas, Texas, June 2015.

[43]Buckley, H. P. and Zingg, D. W., "An Approach to Aerodynamic Design through Numerical Optimization," *AIAA Journal*, Vol. 51, No. 8, August 2013, pp. 1972–1981.

[44]Somers, D. M., "Design and Experimental Results for a Natural-Laminar-Flow Airfoil for General Aviation Applications," Technical Paper 1861, National Aeronautics and Space Administration, June 1981.

[45]Barbarino, S., Bilgen, O., Ajaj, R. M., Friswell, M. I., and Inman, D. J., "A Review of Morphing Aircraft," *Journal of Intelligent Material Systems and Structures*, Vol. 22, No. 9, Jun 2011, pp. 823–877.

[46]Wicke, K., Kruse, M., and Linke, F., "Mission and economic analysis of aircraft with natural laminar flow," *28th International Congress of the Aeronautical Sciences*, No. 2012-1.7.4, Brisbane, Australia, September 2012.

[47]White, F. M., *Viscous Fluid Flow*, McGraw-Hill, Inc., 3rd ed., 2005.

[48]Eppler, R., *Airfoil Design and Data*, Springer-Verlag, New York, 1990.

[49]Gopalarathnam, A., Broughton, B. A., McGranahan, B. D., and Selig, M. S., "Design of Low Reynolds Number Airfoils with Trips," *Journal of Aircraft*, Vol. 40, No. 4, July 2003, pp. 768–775.

[50]Selig, M. S., "Low Reynolds Number Airfoil Design," *VKI Lecture Series: Applied Vehicle Technology (AVT) Panel*, November 2003.